ELECTRO OPTICAL CHARACTERIZATION OF A SILICON MICROSPHERE

by

Ulas Kemal Ayaz

BS, in Physics, Koç University, 2003

Submitted to the Institute for Graduate Studies in
Science and Engineering partial fulfillment of
the requirements for the degree of
Master of Science

Graduate Program in Physics
Bogaziçi University,
September, 2006

ACKNOWLEDGMENTS

I am deeply grateful to my thesis supervisors, Prof. Gülen Aktas and Prof. Ali Serpengüzel for their kind academic support, supervision and motivation during this research with endless tolerance and patience.

I would like to thank my thesis committee members Prof. Yani Skarlatos, Prof. Günhan Dündar and Assistant Prof. Senol Mutlu for their patience in reading the thesis drafts carefully and for making valuable suggestions.

I am deeply grateful to Adnan Kurt for his continous support and invaluable advice, to Onur Akatlar, Abdullah Demir, and Sinan Findik for their close friendship.

In addition, I wish to thank my mother, my father and my brother, and finally Pelin Armutlu for their support, love and patience during my entire time at Koç University. It is to them, I wish to dedicate this thesis.

I would also like to thank Koç University Microphotonics Research Laboratory, PHOREMOST Grant No: EC FP6 – IST – 511616, and NEMO Grant No: FP6 – IST – 003887, for sponsoring my research.

ABSTRACT

ELECTRO OPTICAL CHARACTERIZATION OF A SILICON MICROSPHERE

In today's world, with the development of optoelectronics, metal interconnections are no longer limiting factor for the performance of electronic systems. Replacing the metal interconnections by optical interconnections could provide low power dissipation, low latencies, and high bandwiths. Such optical interconnections rely on the integration of micro-photonics and microelectronics. Having high quality factors, optical microsphere resonators are ideal circuit elements for wavelength division multiplexing. Silicon, as a common semiconductor the building block of the integrated circuits, also is a very important component with its optical properties. We have experimentally observed the shifts in resonance wavelengths of an electrically driven silicon microsphere of 1000 microns in diameter, in the near IR. We have used a distributed feedback (DFB) laser at 1475nm, and applied dc voltages ranging from -17V to 9V to the microsphere and observed the respected shifts in the resonance wavelengths around 0.005 nm to 0.080 nm.

ÖZET

BIR SILIKON MIKROKÜRENIN ELEKTRO-OPTIK KARAKTERISTIGININ ÇIKARILMASI

Günümüz dünyasinda, optoelektronik alanindaki gelismelerle, metal baglantilar elektronik sistemlerin performansini sinirlayici unsur olmaktan çikiyor. Metal baglantilari optik baglantilarla degistirmek, güç kaybini ve bilgi aktarimindaki gecikmeleri düsürüp daha yüksek bant genisliginde bilgi iletimini saglayabilir. Optik baglantilar mikrofotonik ve miktoelektronik alanlarinin bütünlesmesine baglidir. Yüksek kalite faktörleriyle, optik mikroküre çinlayicilarinin dalga bölmek ve çoklamak uygulamalari için ideal devre elemanlari olduklari ispatlanmistir. Yaygin bir yariiletken ve entegra devrelerin yapitasi olan silikon ayni zamanda optik karakteristigi açisindan önemlidir. Bu çalismalarimizda, elektrikle yönlendirilen 1000 mikron çapindaki bir silikon kürenin yakin kizilalti dalga boylarinda, çinlama dalgaboylarindaki degismeleri deneysel olarak inceledik. 1475 nm dalgaboyunda çalisan bir geri besleme lazeri kullanarak -17 V ve 9 V araliginda dogru akimli gerilim uyguladik ve çinlama dalgaboylarinda 0.005 nm'den 0.080 nm'ye varan degisimler gözledik.

TABLE OF CONTENTS

LIST OF FIGURES

LIST OF TABLES

LIST OF SYMBOLS

a	Microsphere radius
a_n	Elastically scattered transverse magnetic field coefficient
b_n	Elastically scattered transverse electric field coefficient
c_n	Internal transverse magnetic field coefficient
d_n	Internal transverse electric field coefficient
$\Delta\lambda$	Mode spacing in wavelength
$\delta\lambda$	Wavelength shift
e	Permittivity of the medium
E	Electric field amplitude
h	Plank’s constant divided by 2π
$h_n^1(x)$	Spherical Hankel function of the first kind
$h_n^2(x)$	Spherical Hankel function of the second kind
$\mathrm{j_n}$ (x)	Spherical Bessel function
k	Wavenumber
k	Imaginary part of the refractive index
L	Spreading length of the Gaussian Beam
l	Mode order
l	Wavelength of light in vacuum
$l_{1/2}$	Linewidth of an MDR
m	Azimuthal mode number
m	Real part of the refractive index
s	Beam confinement parameter of the Gaussian Beam
m	Permeability of the medium
n	Mode number
w	Optical angular frequency
$w_{n,l}$	Resonant angular frequency
p	Momentum of the photon
P_i	Power coupled into an MDR
Q	Quality factor of a MDR

Q_0	Quality factor associated with the internal losses
$Q_{coupling}$	Quality factor associated with the coupling losses
Q_{abs}	Quality factor associated with the absorption losses
Q_r	Quality factor associated with the diffraction losses
Q_s	Quality factor associated with the scattering losses
?	Polar angle
q_{in}	Angle of incidence
q_c	Critical angle
x	Size parameter of the microsphere

1. INTRODUCTION

With the development of optoelectronics, metal interconnections are no longer the limiting factor for the performance of electronic systems. Replacing the metal interconnections by optical interconnections could provide low power dissipation, low latencies and high bandwidths. Such optical interconnections rely on the integration of microphotonics with microelectronics. Microsphere resonators are ideal microphotonic building blocks due to their small volumes and high quality factor (Q-factor) morphology dependent resonances (MDR's), i.e., whispering gallery modes (WGM's) [1, 2] with reported Q-factors ranging up to $2x10^{10}$ [3]. There have been various photonic applications in the ultraviolet (UV), visible and near-infrared (IR) communication bands [4]. Morphology dependent resonances (MDR's), i.e., whispering gallery modes (WGM's), or simply optical resonances of dielectric microspheres provide the necessary optical feedback for applications in spectroscopy, laser science, and optical communications. Microlasers [5], optical filters [4, 6, 7], optical switches [8], ultrafine sensors [9] and rotation detectors [10] are some of the applications of microspheres. Low threshold lasing from rare earth doped silica microspheres [11], polymer microsphere lasers [12] and Raman lasers have been demonstrated. Strain tunable microsphere oscillators [13], add-drop filters [5], and thermooptical switching [8] have been realized for the frequency control in optical communications. Microsphere resonators are uniquely applicable for compact optoelectronic devices in wavelength division multiplexing (WDM) applications [14].

Chapter 2 provides a brief explanation of optical resonators and then gives detailed information necessary to understand the working principles of Fabry-Perot resonators. After understanding the Fabry-Perot resonators, the microsphere as an optical resonator is studied in chapter 2. Lorenz-Mie theory, mode spacing, and Q-factor of the microsphere are overviewed.

In chapter 3, the optical modulation methods for silicon are explained. Starting with a brief overview of the silicon photonics, the effects of electric field and charge injection and the thermal energy on silicon are studied in chapter 3. Finally, a comparison of the modulation methods is included.

Chapter 4 is on the electrical characterization of silicon. Starting with the metal-semiconductor contact, the band diagrams, contact types and the current transportation on a metal-semiconductor junction are given. Following those, the contact that is used in our experiments and the circuits that were used in the electrical input are shown. Finally, the observed current-voltage characteristics for different contacts are presented in chapter 4.

In chapter 5, the evanescent wave coupling techniques are explained. Also, the experimental setup, experimental results of the elastic scattering from a silicon microsphere are presented. The experimental results of elastic scattering from the microsphere when the electrical potential applied are presented and the results are compared.

The thesis is concluded with a short summary of the performed study in chapter 6.

2. OPTICAL RESONATORS

In an optical resonator, light navigates in a closed space with very small loss. In its path, light interferes with itself, and by experiencing constructive interference, a moderate input might build up to high field intensities. There are quite a few optical resonators currently used for various applications. Planar and spherical mirror resonators [15], microrings [16], microdiscs [17], and toroids [18] are the most typical resonators. In addition to the one and two dimensional resonators, microsphere resonators confine the light in three dimensions. [1] The general condition for all the resonators is that, in a round-trip, the light should satisfy the phase matching with the incident beam, such that the phase differences of the incident light and that of the traveled should interfere by a multiple of 2?.

$$?? = 2?n \tag{2.1}$$

where n is the integer mode number. The waves satisfying phase matching interferes constructively, resulting in a series of standing electromagnetic waves. The corresponding phase matching modes determine the resonant wavelengths of the resonator.

2.1. The Fabry-Perot Resonator

The Fabry-Perot resonator is the simplest of the optical resonators. It consists of two highly reflective parallel placed planar mirrors facing each other [15]. In figure 2.1, a simple diagram of the Fabry-Perot resonator is illustrated.

When a plane wave is incident on a plane mirror of 99.9% reflectance, nearly no transmission occurs. However, if two of them are parallel and facing each other, the light making a round-trip between the mirrors and the incident light interferes with each other. The incident light first gets into the resonator, bounces back from the second mirror, travels back to the first mirror and bounces back from it as well, which results with the overlapping of the light that made a full round-trip inside the resonator and the incident beam.

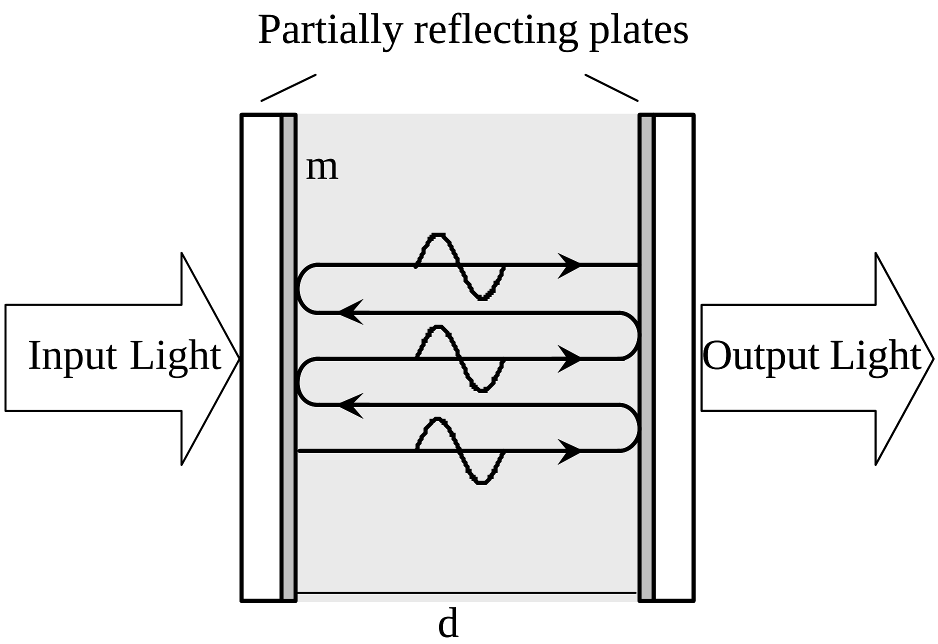

Figure 2.1 The schematic Fabry-Perot resonator

At certain wavelengths, there is no phase difference between those beams, they make a constructive interference, and the intensity of the light inside the resonator doubles. As the light keeps bouncing back and forth from the mirrors with very small transmission at each reflection, the intensity inside the resonator increases, and thus the intensity of the transmitted light go up regardless of the reflectance of the mirrors. The wavelengths satisfying this condition are called the resonance wavelengths.

2.1.1. The Resonator Modes

The physical definition of the resonator modes is the self-consistent existence of the wavefunctions and the resonance wavelengths within the resonator. A mode is a self-reproducing wave that interferes with itself constructively within the resonator, and only self reproducing waves can exist inside the resonator. Resonator modes are subject to the boundary conditions of the Helmholtz equation. Resonant wavelengths are restricted to discrete values, when the equation is solved for standing waves for a Fabry-Perot resonator. Standing wave solution, therefore will give us the equation:

$$n\frac{l_n}{2} = md \tag{2.2}$$

where m is the refractive index of the medium inside the resonator; d is the distance between the mirrors, ? is the vacuum wavelength of the light and n is an integer mode number. Defining a parameter to simplify the above equation:

$$x = \frac{2d}{l} \tag{2.3}$$

We call x the size parameter. Then (2.2) becomes:

$$n = mx \tag{2.4}$$

The waves satisfying (2.1) interfere constructively and form a series of standing electromagnetic waves satisfying equation (2.4). Taking the derivative of (2.2) and dividing it with itself, we can see how the resonant wavelengths change:

$$d\,l \equiv l\left(\frac{dd}{d} + \frac{dm}{m}\right) \tag{2.5}$$

Equation (2.5) gives the sensitivity of the Fabry-Perot resonator. Any change in the distance between the mirrors and the refractive index changes the resonant wavelengths as given in equation (2.5).

If there is no absorption, regardless of the reflectance of the mirrors, the resonator becomes transparent at the resonance wavelengths. The sharpness of the peaks however is dependent on the reflectance of the mirrors.

The quality factor (Q-factor) is given by:

$$Q = 2p \frac{stored \quad energy}{energy \quad loss \quad percycle} \tag{2.6}$$

Quality factor is a measure of the sensitivity of the resonator. In terms of parameters, Q-factor is given as:

$$Q = \frac{l}{\Delta l_{1/2}} \tag{2.7}$$

where ?$_{1/2}$ is the full width half maximum (FWHM) of the resonance.

The quality factor determines the sharpness of the resonance. Q-factor may also be called the resolving power of the resonator. As the reflectance of the mirrors increase, the energy loss per cycle decrease; therefore the quality factor increases with the reflectance of the mirrors. In most of the filter applications, high Q-factor is a desirable parameter.

The resonance condition given by equation (2.2) satisfies infinite number of resonance modes. The difference between the resonance wavelengths of adjacent resonance modes is called free spectral range (FSR). The distance between adjacent resonances has consecutive mode number n. The FSR then is given with the expression:

$$\Delta l_{FSR} = \frac{l_n}{n} - \frac{l_{n+1}}{n+1} \tag{2.8}$$

From equation (2.2), replacing the wavelength:

$$\begin{aligned} \Delta l_{FSR} &= \frac{2md}{n} - \frac{2md}{n+1} \\ &= \frac{2md}{n(n+1)} \end{aligned} \tag{2.9}$$

For n being large, we can make the approximation of n+1˜ n, on (2.9) which would make:

$$\Delta l_{FSR} = \frac{2md}{n^2} \tag{2.10}$$

by using (2.2) once more:

$$\Delta l_{FSR} = \frac{l^2}{2md} \tag{2.11}$$

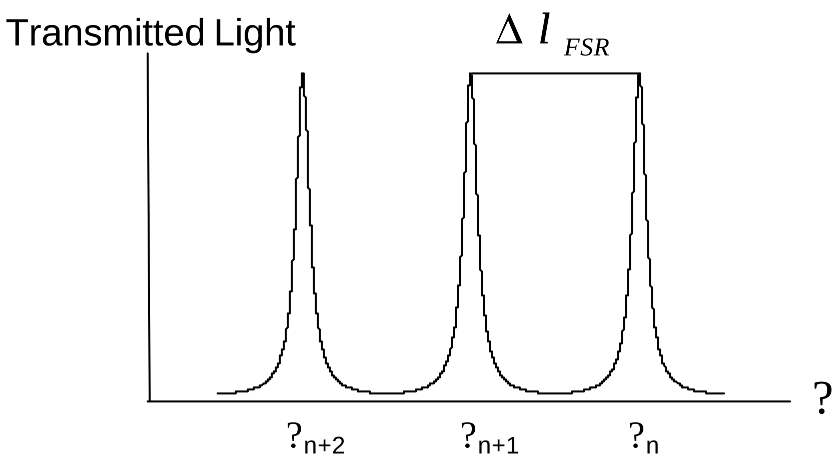

Figure 2.2. Expected intensity of the transmitted light in a Fabry-Perot resonator

An illustration of the intensity of the output beam from the Fabry-Perot resonator is given in figure 2.2, in which the mode spacing ??$_{FSR}$ can be seen along with the adjacent resonance wavelengths. As it can be seen in equation (2.11), the FSR in Fabry-Perot resonator is inversely proportional to the distance between of the parallel mirrors. The dependence of FSR on the distance of the mirrors is also calculated in figure 2.3, for mediums of glass (m = 1.5) and silicon (m = 3.5).

The ratio of the FSR to the linewidth of the resonance is called finesse (F), which can be expressed as:

$$F = \frac{\Delta l_{FSR}}{\Delta l_{1/2}} \tag{2.12}$$

For a Fabry-Perot resonator, the expression for finesse is given as:

$$F = \frac{p\sqrt{R}}{1-R} \tag{2.13}$$

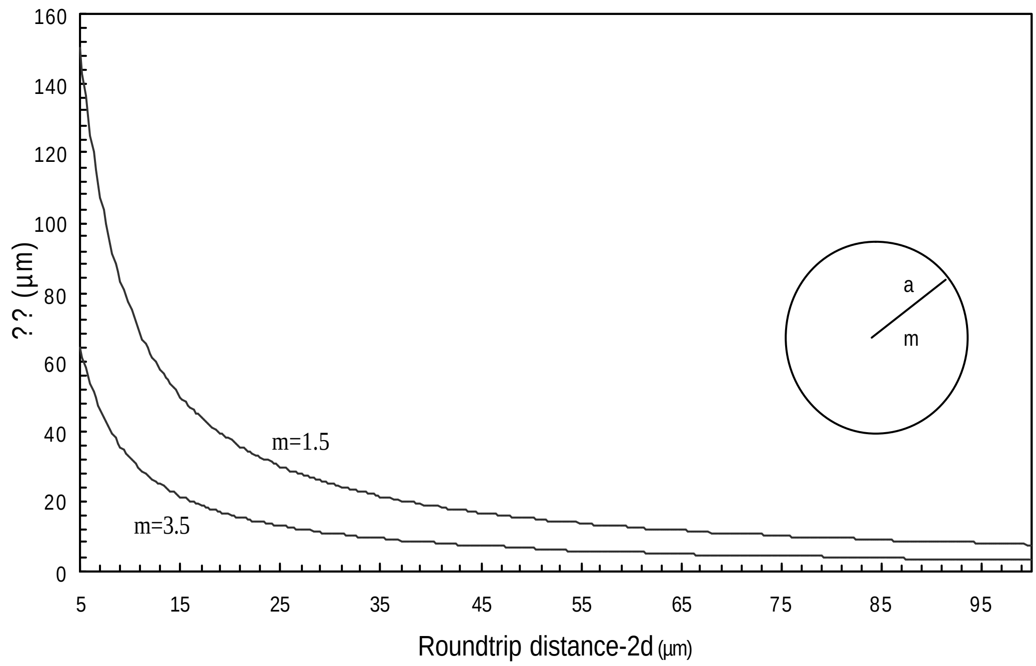

Figure 2.3. The dependence of FSR on round-trip distance for a Fabry-Perot resonator

where R is the reflectance of the mirrors in the Fabry-Perot resonator. In light of equation (2.7) for Q-factor and (2.12) for finesse, the Q-factor in terms of finesse would be given as:

$$Q = \frac{l}{\Delta l_{FSR}} F = nF \qquad (2.14)$$

Equation (2.13) can be revised to write the Q-factor in terms of reflectance, index of refraction, and the size parameter. Using the equations for size parameter, FSR and finesse as given in equation (2.3), (2.11) and (2.13):

$$Q = \frac{mxp\sqrt{R}}{1 - R} \qquad (2.15)$$

Now increasing reflectance, size parameter or the internal refractive index of the resonator, the Q-factor becomes higher, leading to sharper peaks and higher resolving power of the resonator. From the equation (2.4) of the resonator modes, increasing the refractive index and the size parameter leads to higher order modes. Therefore, higher order modes also lead to high Q-factor resonances.

2.1.2. The Resonance Phase and Intensities

In an optical resonator, the light beam interferes with itself repeatedly. When the interference is constructive and the resonance condition is satisfied, the result of the superposition may become an infinite number of waves. Consider now that the incident beam is given as E_0e^{iwt}, and let E_t represent the total transmitted wave [22]. At each reflection from the mirrors, there will be a coefficient of r for reflection amplitude of coefficient will add up to the incident beam. For transmission amplitude, there will be a coefficient of t adding up to the incident beam. The superposition of the waves will be given as:

$$E_t = E_{1t} + E_{2t} + \ldots\ldots + E_{Nt}$$

$$= E_0t^2e^{iwt} + E_0t^2r^2e^{i(wt-d)} + E_0t^2r^4e^{i(wt-2d)} + \ldots + E_0t^2r^{2(N-1)}e^{i[wt-(N-1)d]}$$

$$= E_0Te^{iwt}\,[1+R\,e^{-id} + R\,e^{-i2d} + \ldots + R^{(N-1)}\,e^{-i(N-1)d}] \qquad (2.16)$$

T and R are transmittance and reflectance of the surfaces, and they are squares of the coefficients t and r respectively; in the case of no absorption, they add up to unity. The superposition of waves in equation (2.15), when there is infinite number of waves, add up to:

$$E_t = E_0 e^{iwt}\left(\frac{T}{1-\mathrm{Re}^{-id}}\right) \tag{2.17}$$

The difference between each adjacent transmission is a phase difference imposed on the wave. Since the light is traveling back and forth and interfering with itself, the optical path difference will impose a phase difference on the interfering waves. The difference in optical path for a Fabry-Perot resonator is:

$$d = 2mdk_0 = \frac{2mdp}{l} = mxp \tag{2.18}$$

where k_0 is the wavenumber of the incident light. The difference between resonances corresponds to a phase difference 2?. The field, in general can be written as:

$$E = E_0 e^{i(wt+f)} \tag{2.19}$$

The phase difference ? given in (2.19) can be derived from the equation (2.17):

$$e^{if} = \left(\frac{T}{1-\mathrm{Re}^{id}}\right) \tag{2.20}$$

Which we can write as:

$$\tan f = \frac{\mathrm{Im}\left(\frac{T}{1-\mathrm{Re}^{id}}\right)}{\mathrm{Re}\left(\frac{T}{1-\mathrm{Re}^{id}}\right)} \tag{2.21}$$

and taking out the phase alone:

$$f = \arctan\left(\frac{\sin d}{\left(\frac{1}{R}\right) - \cos d}\right) \tag{2.22}$$

The phase in (2.22) is a function of the optical path difference and reflectance alone. The necessary condition for resonances to occur is to have multiples of 2? for the phase difference. Once the field inside the resonator is found, the intensity of the incident light and the transmitted light can be calculated, provided the reflectance of the mirrors and the separation of mirrors within the resonator are known.

Consider an incident beam with the intensity equal to I_{inc}. When the light makes the first contact with the resonator, a fraction of the beam will enter the resonator. When the beam makes a contact with the second mirror, again only a fraction of the light will transmit and the rest will be reflected back into the resonator.

To put it more numerically, the intensity of a beam with the field E is given as:

$$I_{inc} \propto \frac{E.E^*}{2n} = \frac{E_0^2}{2n} \tag{2.23}$$

After the light gets into the resonator, the intensity of the transmitted beam:

$$I_t = \frac{I_{inc}}{1 - 2R\cos d + R^2}$$

$$= \frac{I_{inc}}{1 - 2R\left[1 - 2\sin^2\left(\frac{d}{2}\right)\right] + R^2}$$

$$I_t = \frac{I_{inc}.T^2}{(1-R)^2 + 4R\sin^2\left(\frac{d}{2}\right)} \tag{2.24}$$

From the intensity of the wave inside the resonator, the intensity of the transmitted wave can be derived. The light inside the resonator will bounce from the mirrors, each time multiplying the intensity by T, which is equal to 1-R. Therefore the transmitted light can be expressed as:

$$\frac{I_t}{I_{inc}} = \frac{.(1-R)^2}{(1-R)^2 + 4R\sin^2\left(\frac{d}{2}\right)}$$

$$T(d) = \frac{I_t}{I_{inc}} = \left(\frac{1}{1+\frac{4R}{(1-R)^2}\sin^2\left(\frac{d}{2}\right)}\right) \tag{2.25}$$

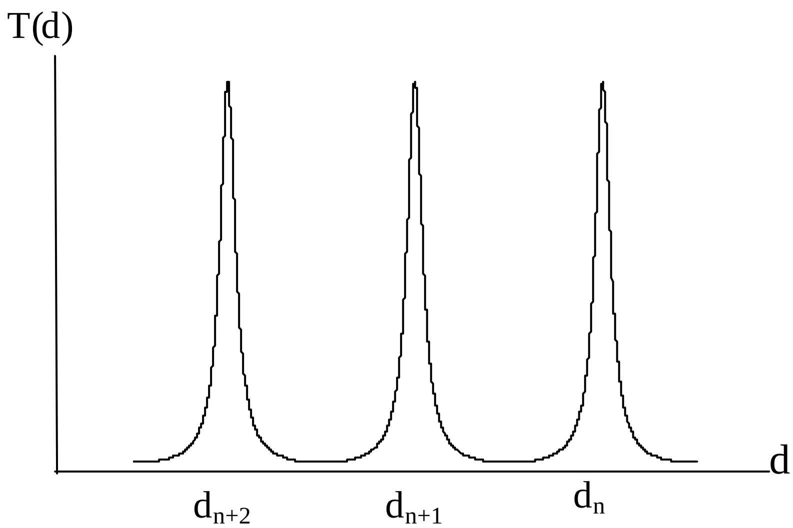

Figure 2.4. Expected transmittance of a Fabry-Perot resonator with highly reflecting mirrors

In the case of resonance, that is, when the phase difference is zero or multiples of 2?, the transmission becomes unity, meaning the mirrors becomes transparent and the incident light is totally transmitted. The reflected light intensity can also be found from equation (2.25):

$$R = 1 - T = 1 - \left(\frac{1}{1 + \frac{4R}{(1-R)^2} \sin^2\left(\frac{d}{2}\right)} \right) = \frac{\frac{4R}{(1-R)^2} \sin^2\left(\frac{d}{2}\right)}{1 + \frac{4R}{(1-R)^2} \sin^2\left(\frac{d}{2}\right)} \tag{2.26}$$

which will be zero when the phase difference is zero.

The transmittance and reflectance can also be written in terms of size parameter. By using equation (2.18) we can write T and R as:

$$T(d) = \frac{I_t}{I_{inc}} = \left(\frac{1}{1 + \frac{4R}{(1-R)^2} \sin^2\left(\frac{mpx}{2}\right)} \right) \tag{2.27}$$

$$R = 1 - T = \frac{\frac{4R}{(1-R)^2} \sin^2\left(\frac{mpx}{2}\right)}{1 + \frac{4R}{(1-R)^2} \sin^2\left(\frac{mpx}{2}\right)} \tag{2.28}$$

The analysis of Fabry-Perot resonator is important in understanding the general properties of optical resonators. We will see next the microsphere as an optical resonator for example, and we will see similarities in their working principles.

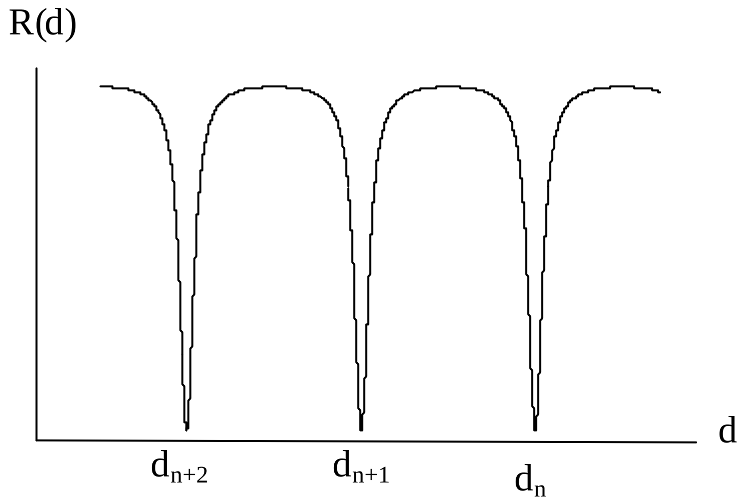

Figure 2.5. Expected reflectance of a Fabry-Perot resonator with highly reflecting mirrors

2.2. The Microsphere Resonator

Gustav Mie was the first scientist to investigate the morphology dependent resonances (MDR's) of microspheres, in the beginning of 19^{th} century [19]. The intuition leading to the basic idea of the microsphere resonator's working principle is based on the geometric optics. In investigating the light scattering from spherical particles, the resonant circulation of optical field inside the microsphere caused the spectrum to give sharp responses. These optical modes are called "whispering-gallery modes", which originated from the phenomenon of acoustic waves observed propagating in the interior surface of the Saint Paul's Cathedral in London, observed and published by Lord Rayleigh [19].

As an optical resonator, the microsphere has its similarities with the Fabry-Perot resonator. The obvious difference isthat, instead of the area within the mirrors, the cavity is determined by the interior surface of the microsphere. A physical interpretation of MDR's is based on the propagation of rays around the inside surface of the microsphere, confined by an almost total internal reflection (TIR). The rays approach the interior surface of the microsphere at an angle beyond the critical angle, they bounce off from the interior surface of the sphere, and as the light continues its path inside the sphere, all subsequent angles of incidence are the same because of the spherical symmetry, and the ray is trapped. The trapped ray propagates close to the surface, and traverses a distance ≈

$2\pi a$ in one round trip [23]. Once the light returns to its respective entrance points, it starts to propagate in the interior surface of the microsphere all over again. This basically is the physical interpretation of the MDR’s for a microsphere. The light, after circumnavigating the interior surface of the sphere, returns to its entrance point and interferes with itself. At resonant wavelengths, the interference is constructive and the interference might result in standing waves, causing the elastically scattered light from the microsphere to reach peak intensities. Numerically, using the similar expression from the Fabry-Perot resonator in equation (2.2) the condition of resonance would be:

$$n l \approx m 2pa \tag{2.29}$$

Similarly, for the size parameter:

$$x = \frac{2pa}{l} \tag{2.30}$$

Which, we can use to write 2.29 as:

$$n = mx \tag{2.31}$$

The geometrical ray optics definition of MDRs of a microsphere fails to explain the following significant points: How is the light coupled into the microsphere, and how does the light escape from the microsphere? Furthermore, the geometrical ray optics does not take polarization of the light into account, and is not sufficient to determine the radial character of the optical modes [20]. In order to pass the limitations imposed by the ray optics, we need to examine the Lorenz-Mie Theory.

2.2.1. Lorenz-Mie Theory

The interaction of light with a microsphere can be explained by using Lorenz-Mie theory. According to this theory, the light waves are expressed as the superposition of the electromagnetic waves. From there, the characteristic equations for the MDRs are derived by imposing the appropriate boundary conditions for the fields.

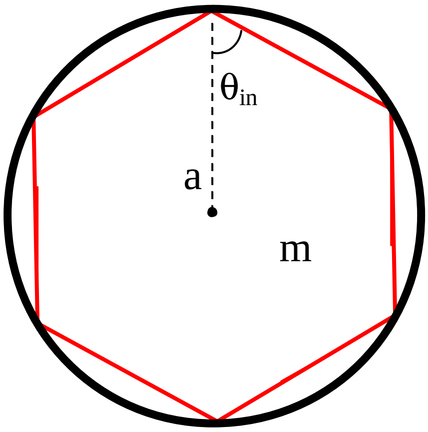

Figure 2.6. An illustration of optical resonance path
inside the microsphere

As has been studied in the Fabry-Perot resonator, and seen in the equation (2.28) the MDR's occur at discrete wavelengths depending on the refractive index of the cavity and the optical path length. The characteristic equations are obtained by expanding the fields in vector spherical harmonics and then matching the tangential components of the electric and magnetic fields at the surface of the sphere. As in the spherical harmonics, the MDRs will have the quantum numbers labeled as polar mode number (n), azimuthal mode number (m), and radial mode order (l). For a perfect sphere, all of the m modes are degenerate (with $2n+1$ degeneracy) [19, 24]. The degeneracy is partially lifted when the cavity is axisymmetrically (along the z-axis) deformed from sphericity. For such distortions the integer values for m are $\pm n$, $\pm(n-1),\ldots,0$, where the degeneracy remains, because the resonance modes are independent of the circulation direction.

The resonances inside the microsphere are characterized by their polarization: transverse electric (TE), and transverse magnetic (TM). For optical modes having TM polarization, the characteristic equation is:

$$\frac{\left[mxj_n(mx)\right]'}{j_n(mx)} = \frac{\left[xh_n^{(1)}(x)\right]'}{h_n^{(1)}(x)} \tag{2.32}$$

Whereas, the characteristic equation for TE modes is:

$$\frac{[mj_n(mx)]'}{m^2 j_n(mx)} = \frac{[xh_n^{(1)}(x)]'}{h_n^{(1)}(x)} \tag{2.33}$$

where for both (2.29) and (2.30) the $j_n(x)$ and $h_n^{(1)}(x)$ are the spherical Bessel and the Hankel functions of the first kind, respectively. The prime in the equation denotes the differentiation with respect to the argument.

The elastically scattered field can be written as an expansion of vector spherical wave functions with TM coefficients (a_n) and TE coefficients (b_n) for a plane wave. The expansion coefficients for the scattered TM field are given as [25]:

$$a_n = \frac{j_n(x)[mxj_n(mx)]' - m^2 j_n(mx)[xj_n(x)]'}{h_n^{(2)}(x)[mxj_n(mx)]' - m^2 j_n(mx)[xh_n^{(2)}(x)]'} \tag{2.34}$$

and the coefficients for TE field are given as:

$$b_n = \frac{j_n(x)[mxj_n(mx)]' - j_n(mx)[xj_n(x)]'}{h_n^{(2)}(x)[mxj_n(mx)]' - j_n(mx)[xh_n^{(2)}(x)]'} \tag{2.35}$$

where j_n is the spherical Bessel function, and $h_n^{(2)}$ is the spherical Henkel function of the second kind [26]. The natural resonance frequencies associated with TE and TM modes are given by:

$$w_{n,l} = \frac{x_{n,l}}{a\sqrt{me}} \tag{2.36}$$

where μ is the permeability and ε permittivity of the surrounding lossless medium. The coefficients a_n and b_n become infinite, when there is a complex frequency corresponding to complex size parameter. The MDR's of the microsphere occur at the zeros of the denominators of a_n and b_n coefficients, given by equations (2.34) and (2.35) [27]. The modes are radiative for real frequencies, and hence the modes are virtual and the resonance frequencies are complex. The real part of the pole frequency is close to real resonance frequency, $w_{n,l}$ [28]. The imaginary part of the pole frequency determines the linewidth of the resonance, $w_{1/2}$. [29, 30]

2.2.2. Q-factor

The performance of a resonator can be determined by quality factor (Q-factor) as was seen for the Fabry-Perot resonator. The Q-factor of an optical resonator determines how long a photon can be stored inside an MDR [31]. Therefore the Q-factor of a resonance is governed by the losses in the optical field during the round-trip associated with it, and the losses in coupling the light into the sphere. The losses during the round-trip can be labeled as: the loss due to the absorption of the sphere (Q_{abs}), the loss due to the diffraction leakage (Q_r) and finally, the loss caused by the scattering (Q_s), and the loss due to coupling ($Q_{coupling}$). The observed Q-factor is the geometric sum of the Q-factors associated with each mechanism:

$$\frac{1}{Q} = \frac{1}{Q_{abs}} + \frac{1}{Q_r} + \frac{1}{Q_s} + \frac{1}{Q_{coupling}} \tag{2.37}$$

For frequencies near an MDR, the electric field inside the microsphere varies as:

$$E(t) = E_0 \exp(-iw_0 t - \frac{w_o}{2Q} t) \tag{2.38}$$

The intensity of the field is proportional to:

$$\left|E(w)\right|^2 \propto \frac{1}{(w - w_0)^2 + (w_0 / 2Q)^2} \tag{2.39}$$

As seen in equation (2.34), the Q-factor determines the sharpness of the resonance peaks. The Q-factor and wavelengths of MDR's of microspheres are highly sensitive functions of size and refractive index. The higher the Q-factor, the more sensitive is the microsphere to the perturbations.

2.2.3. Mode Spacing of MDR's

From equations (2.26), (2.27) and (2.28), we saw that an MDR satisfies resonance condition for specific values of the size parameter. The mode spacing (? ?) then, is defined as the wavelength difference between two consecutive mode numbers (n) in the same mode order (l) [32]:

$$\Delta l_{n,l} \equiv l_{n+1,l} - l_{n,l} \tag{2.40}$$

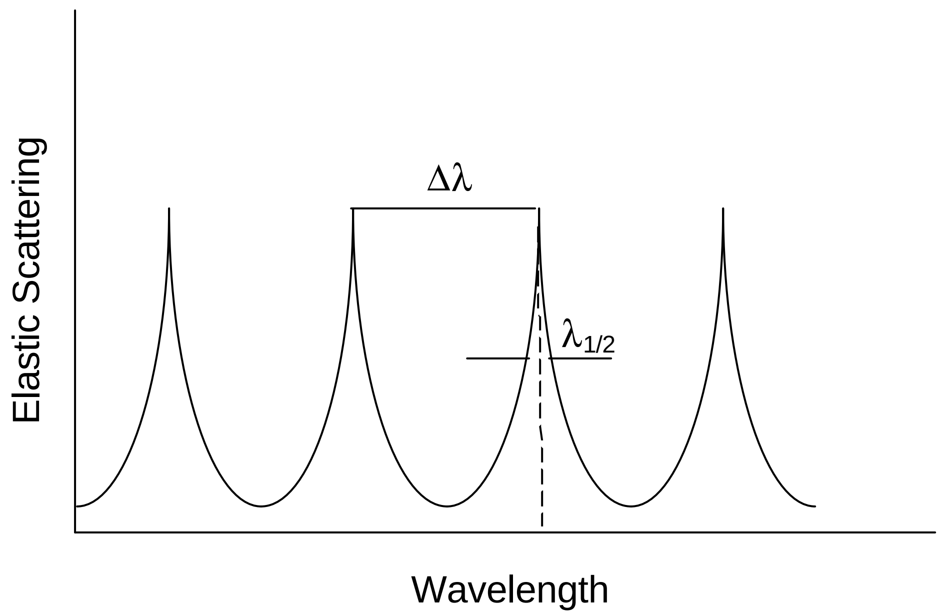

Figure 2.7. Expected intensity of elastic scattering from microsphere resonator

$$\Delta l = \frac{l^2}{2pa} \frac{\tan^{-1}(\sqrt{m^2 - 1})}{\sqrt{m^2 - 1}} \tag{2.41}$$

Mode spacing of the microsphere resonator, as can be seen from equation (2.38), resembles the FSR of the Fabry-Perot resonator from equation (2.11). The only difference in between the equations is the index of refraction of the resonators. Therefore, we can introduce a new parameter for microsphere resonator:

$$m_{eff} = \frac{\sqrt{m^2 - 1}}{\tan^{-1}(\sqrt{m^2 - 1})} \tag{2.42}$$

m_{eff} given here is defined as the effective index of refraction of a microsphere resonator. From equation (2.35), we can deduce that the closer the unity the index of refraction is, the closer the mode spacing of a microsphere and Fabry-Perot resonator.

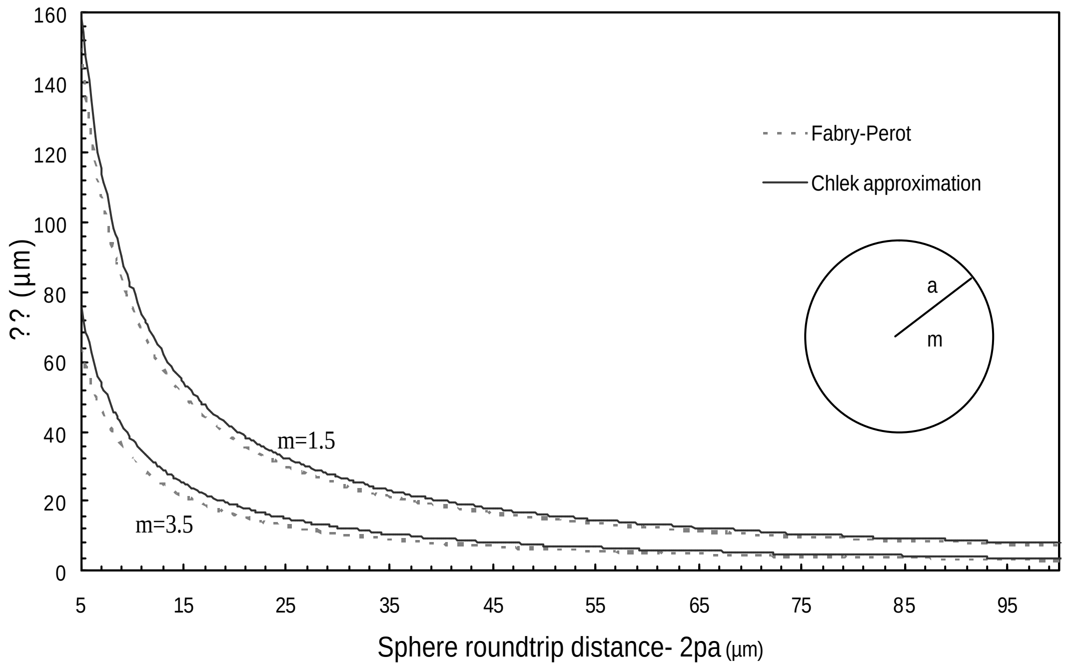

Figure 2.8. Mode spacing of microsphere and Fabry-Perot resonators as a function of round-trip distance (2?a)

Figure 2.8 illustrates calculations of mode spacing as a function of the round-trip distance for microsphere and Fabry-Perot resonators. The calculation is for glass (m = 1.5) and silicon (m = 3.5). It can be seen from the graph, that the difference in mode spacing is closer for glass, than that of silicon at optical frequencies.

3. ELECTRO-OPTIC EFFECTS IN SILICON

3.1 Silicon Photonics

Silicon has been the material of choice for the solid state microelectronics industry for more than fifty years. [7] For microelectronics applications, silicon chip design has many applications and is the basis of complex microprocessors and integrated circuits.

Currently, it is a question whether silicon can be the material of choice in the photonic integrated circuits. Although silicon photonics is less well-developed than that of group III-V semiconductors, being low-cost and highly available, as well as being well-understood in electronics [33, 34], silicon photonics can make a real impact in the optical communications [35].

There are significant challenges for using the silicon photonics. Silicon has an indirect bandgap, making it an inefficient light emitter [36]. Silicon is transparent at the telecom spectral regions of 1.3 µm and 1.55 µm. Finally, optical interconnections require precise alignment, which require improved alignment technologies for mass production.

Silicon also has substantial advantages in photonics. First, silicon is suitable for guiding light in waveguides without excessive loss. The transparency range of silicon extends from 1.1 µm to well into the far-infrared region. Second, silicon's Raman gain coefficient is high and with the efficient use of waveguides, the light can be confined in a small area, thus allowing for efficient Raman amplification [37, 38]. Recently, Raman scattering in pulsed and continuous-wave [39] silicon Raman lasers have been observed. The downside is that a Raman laser or amplifier still requires an optical pump source. Another progress of silicon photonics is the silicon optical modulators. Using a Mach-Zehnder interferometer, changing the charge density in one arm of the interferometer by applying an electrical input causes a change in the refractive index, which modulates the phase of the output beam [34]. Silicon photonics still require an enormous amount of work corresponding to substantial investments. However, the potential merits of the technology are highly motivative. If successful, it can lead to a powerful technology with substantial benefits for microphotonics and microelectronics applications.

3.2. Optical Modulation Mechanisms in Silicon

For integrated optical technology, one of the requirements is the ability to perform optical modulation, which is basically a change in the optical field due to an applied external signal. Usually, the change in the optical field is derived from the change in the refractive index of the material, though it is possible to make modulation by other parameters. For silicon, the most efficient means of implementing optical modulation by an applied electrical signal is to use carrier injection or depletion. There are other methods for optical modulations, which are not as effective in silicon but are used for other integrated optical technologies. These electrically driven modulation techniques are primarily based on electric field effects.

Applying an electric field to a material can result in a change to both the real refractive index and the imaginary refractive index. The change in the real part refractive index of the material due to an applied electric field is labeled as electrorefraction; whereas the change in the imaginary part of the refractive index due to an applied electric field is called electroabsorption. ?m denotes the change in the real refractive index, whereas ?k denotes the change in the imaginary part of the index of refraction. The primary effects known for optical modulation driven by electric field are Pockels effect, Kerr effect, and Franz-Keldysh effect.

3.2.1. The Pockels Effect

The Pockels effect causes a change in the real part of the refractive index that is linearly dependent on the applied electric field, E. If the applied E field is uniform, and the modulator geometry is fixed, the change in the refractive index will be proportional to the applied potential difference. In general, the Pockels effect generates a change in the refractive index that is dependent on the direction of the applied E field with respect to the axes of the modulator crystal. Therefore, the effect is also polarization dependent.

Silicon's symmetry is such that, the Pockels effect disappears completely [34]. The largest electro-optic coefficients, however, can be utilized for other semiconductor materials by aligning the applied field with one of the principal axes. To illustrate, for the material lithium niobate ($LiNbO_3$) the change in the refractive index is given by:

$$\Delta m = -r_{33} m_{33} \frac{E_3}{2} \tag{3.1}$$

where m_{33} is the refractive index in the direction of the applied field, and E_3 is the electric field applied on the material. The subscript 3 is to show that which of the three principal axes, the electric field is aligned with. The value of r_{33} is 30.8 x 10^{-12} m/V.

3.2.2. The Kerr Effect

The Kerr effect also causes a change in the real part of the refractive index. It is a second order effect and is proportional to the square of the applied electric field, E. It is a relatively weak effect in silicon, and the change in ? m may be expressed as:

$$\Delta m = s_{33} m_0 \frac{E^2}{2} \quad (3.2)$$

s_{33} is the Kerr coefficient, m_0 is the unperturbed refractive index and E is the electric field. As it can be seen from the expression, the change in the refractive index is independent of the direction of the applied field. Figure 3.1, shows graph of the change in the refractive index for silicon at 1300 nm due to Kerr effect, which is calculated by Soref and Bennett [39] theoretically.

3.2.3. The Franz-Keldysh Effect

The Franz-Keldysh effect changes both the real part and the imaginary part of the refractive index, although mostly the latter [34]. Upon applying the electric field, the energy bands of the semiconductor experience a distortion, and this shifts the energy bandgap which results in the absorption of the material particularly at wavelengths close to its bandgap.

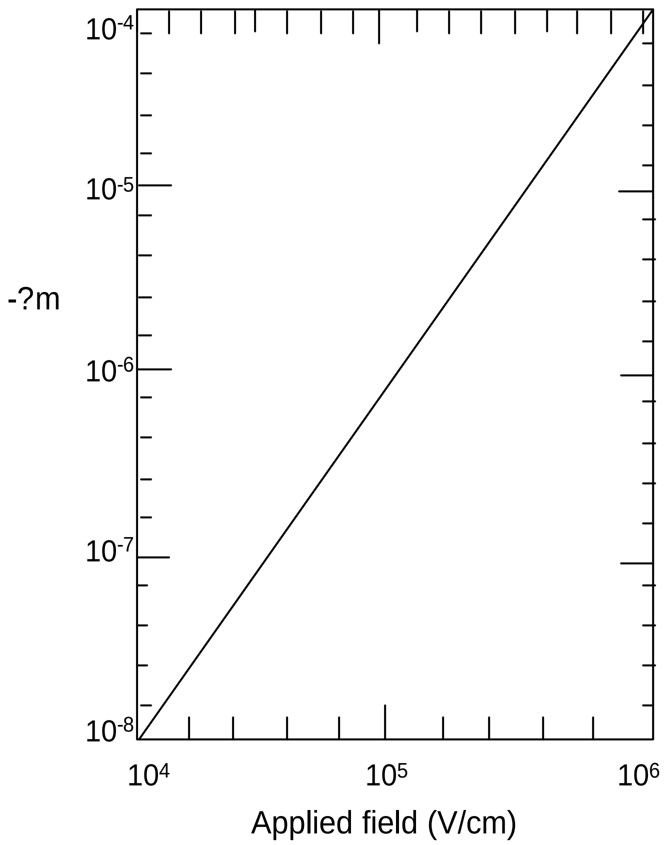

Figure 3.1. The Kerr effect in silicon as a function of applied electric field at 1.3 µm wavelength. Source: Soref and Bennett [39]

The Franz-Keldysh effect is mainly dominant at wavelengths close to the material's bandgap. Soref and Bennett also theoretically calculated the change in the refractive index of the silicon due to the Franz-Keldysh effect [40], which is shown in figure 3.2. The data is calculated for wavelengths of 1.07 µm and 1.09 µm. For silicon, as the wavelength shifts to 1.3 µm and 1.55 µm, the effect of the Franz-Keldysh diminishes significantly.

As it can be seen from the figure, the change in the refractive index reaches to 10^{-4} at an applied field of 10^5 V/cm. This is a bigger shift when it is compared to the Kerr effect however it is evaluated at different wavelengths. At the wavelengths of 1.3 µm and 1.55 µm, the Franz-Keldysh effect diminishes significantly.

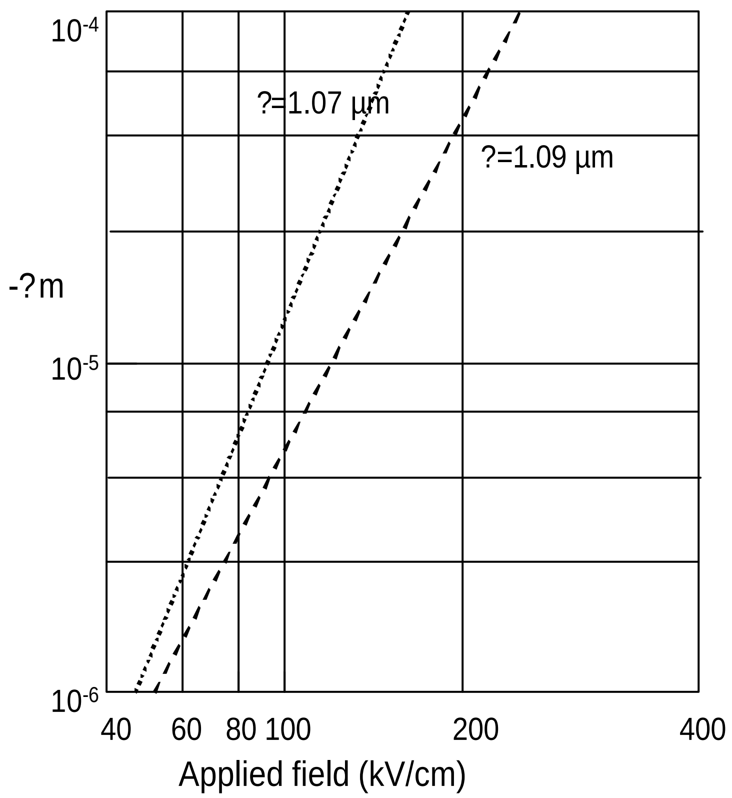

Figure 3.2. The Franz-Keldysh effect in silicon as a function of applied electric field for wavelengths of 1.07 µm and 1.09 µm wavelength. Source: Soref and Bennett[39]

3.2.4. Carrier Injection or Depletion

Changing the concentration of free charges in a semiconductor material can also cause a change in the refractive index of the material. Drude-Lorenz equation, regarding the concentration of free charges to the absorption of the material is:

$$\Delta k = \frac{e^3 l_0^2}{4pc^3 e_0 n}\left(\frac{N_e}{m_e\left(m_{ce}^*\right)^2} + \frac{N_h}{m_h(m_{ch}^*)^2}\right) \tag{3.3}$$

Where N_e and N_h are concentration of electrons and holes, respectively. Meanwhile, the corresponding equation for the change in the real part of refractive index is:

$$\Delta m = \frac{-e^2 l_0^2}{8p^2 c^2 e_0 n}\left(\frac{N_e}{m^*_{ce}} + \frac{N_h}{m^*_{ch}}\right) \tag{3.4}$$

Soref and Bennett studied the dependence of electron and hole densities of silicon on the refractive index experimentally, especially concentrating their work on communication wavelengths of 1.3 µm and 1.55 µm. They found out that their results are related to Drude-Lorenz model for electrons, whereas, for holes there is a dependence of $(?N)^{0.8}$. They have produced the following expressions evaluating the changes in the refractive index of silicon due to carrier injection or depletion at communication wavelengths of 1.3 µm and 1.55 µm.

For ? = 1.55 µm.

$$\begin{aligned} ?m &= ?m_e + ?m_h = -[8.8 \text{ x } 10^{-22}\ ?N_e + 8.5 \text{ x } 10^{-18}\ (?N_h)^{0.8}] \\ ?k &= ?k_e + ?k_h = 8.5 \text{ x } 10^{-18}\ ?N_e + 6.0 \text{ x } 10^{-18}\ ?N_h \end{aligned} \tag{3.5}$$

For ? = 1.3 µm:

$$\begin{aligned} ?m &= ?m_e + ?m_h = -[6.2 \text{ x } 10^{-22}\ ?N_e + 6.0 \text{ x } 10^{-18}\ (?N_h)^{0.8}] \\ ?k &= ?k_e + ?k_h = 6.0 \text{ x } 10^{-18}\ ?N_e + 4.0 \text{ x } 10^{-18}\ ?N_h \end{aligned} \tag{3.6}$$

where $?m_e$ and $?m_h$ are change in the refractive index of silicon due to a change in the electron and hole concentrations; whereas $?k_e$ and $?k_h$ are change in the absorption coefficient of silicon due to a change in the electron and hole concentrations, respectively.

To give an example, consider silicon that has a carrier injection of 10^{15} available. The change in the refractive index of the material at the communication wavelength of 1.55 µm is:

$$? m = -[8.8 \times 10^{-22} (10^{15}) + 8.5 \times 10^{-18} (10^{15})^{0.8}] = 9.4 \times 10^{-6}$$

It is nearing to a change in the order of 10^{-5}. We will see in the upcoming chapters that in our experiments, we have observed a shift in the resonance wavelength of a silicon microsphere that nearly corresponds to such a change in the refractive index. Furthermore, by appropriate doping of the silicon, it is possible to see higher carrier injection levels and thus observe a bigger change in the refractive index.

3.2.5 The Thermo-optic Effect

In addition to the electric field effects and carrier injection-depletion effects on silicon, the thermo-optic effect has also been proven to be viable for optical modulation of silicon. [41] In this method, the index of refraction of silicon is changed by applying heat on the material. The refractive index change of silicon is given by:

$$\frac{dm}{dT} = 1.86x10^{-4} / K \tag{3.7}$$

The problem with the application of this effect though rises from controlling the temperature rise to the locality of the waveguide, and of the efficiency of the mechanism that will deliver the thermal energy. Note that the refractive index change is positive with the applied thermal energy, whereas the carrier injection-depletion effect and also the electric field effects caused a negative change in the refractive index. Therefore, it should be taken into consideration in the design not to compete such effects against each other.

The effects changing the refractive index of the silicon are summarized in table 3.1. The shift in the wavelength corresponds to the shift in the refractive index as is given in equation (2.5). For reference, a light beam of 1475 nm coupled into a silicon microsphere of 1 mm diameter is taken, and the expected resonance wavelength shifts corresponding to the change in the refractive index of the material are calculated. Since the wavelength of the reference light is well above 1.3 µm and nearing the communication band, we have neglected the Franz-Keldysh effect in our calculations.

Table 3.1. Refractive index and wavelength shift for silicon

Silicon Sphere a= 500 micrometers	m=3.48	? =1475nm
	? m	? ?
Pockels Effect (effective)	-5.33×10^{-5} /V	-0.02 nm/V
Kerr Effect	-1.110×10^{-14} /V	-0.047×10^{-10} nm/V
Carrier Injection	-0.71×10^{-3} /V	-0.3 nm/V
Thermo-Optic Effect	1.86×10^{-4} /K	0.07 nm /K

For the carrier injection effect, we have assumed an injection of 10^{15} free charges. Note that the dominating factor in the table is the carrier injection effect. The Kerr Effect is very dim for small electric fields, but would be more significant for higher order fields. Because of the geometry of the silicon crystal, the Pockels effect disappears completely. However, it has been proven that growing a non-symmetric layer on silicon allows the application of Pockels effect [42]. The Pockels effect given in the table is calculated as assuming our silicon microsphere's geometry allowed it, therefore we used our parameters in the calculations.

4. ELECTRICAL CHARACTERIZATION OF THE SILICON MICROSPHERE

When a metal is making contact with a semiconductor, a barrier will be formed at the metal-semiconductor interface [43, 44]. The basic energy diagram showing such a barrier is illustrated in figure 4.1. The Fermi levels of metal and semiconductor in contact must be coincident at thermal equilibrium. At the far the metal and semiconductor are not in contact, and the system is not in thermal equilibrium as can be seen from the difference of the Fermi energy level. If a wire is connected between the metal and the semiconductor, so that charge would flow from the semiconductor to the metal and thermal equilibrium would be established, the Fermi levels on both sides line up [45]. The work function is the energy difference between the vacuum level and the Fermi level. The potential difference between the metal and semiconductor is called the contact potential.

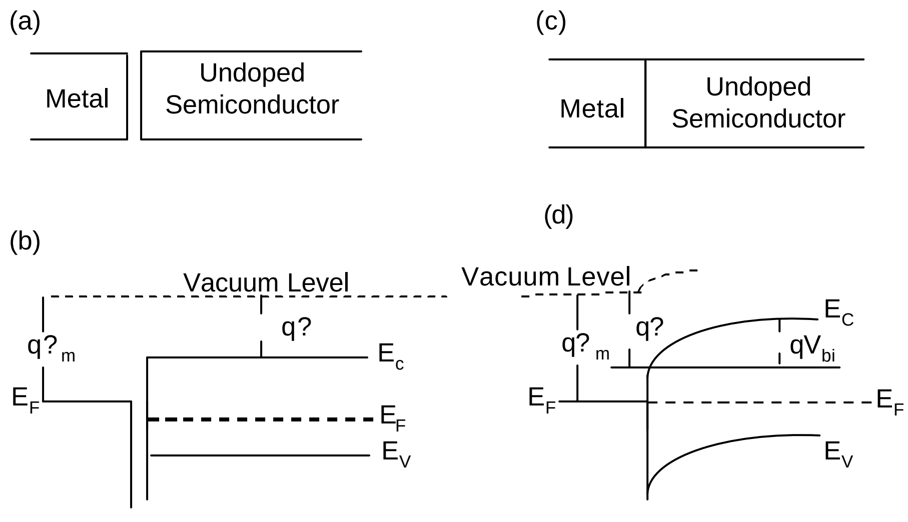

Figure 4.1. a) One dimensional structure of a metal-semiconductor before contact, b) Energy band diagram of a p-type semiconductor under non-equilibrium condition, c) One dimensional structure of a metal-semiconductor contact d) Energy band diagram of metal-semiconductor contact under thermal equilibrium

When a metal and a semiconductor is brought into intimate contact, the conduction and the valence bands of the semiconductor are brought into a definite energy relationship with the Fermi level of the metal. Once known, this relationship serves as the boundary condition [46]. The energy-band diagrams for metals on both n-type and p-type materials are shown in figure 4.2 under different biasing conditions.

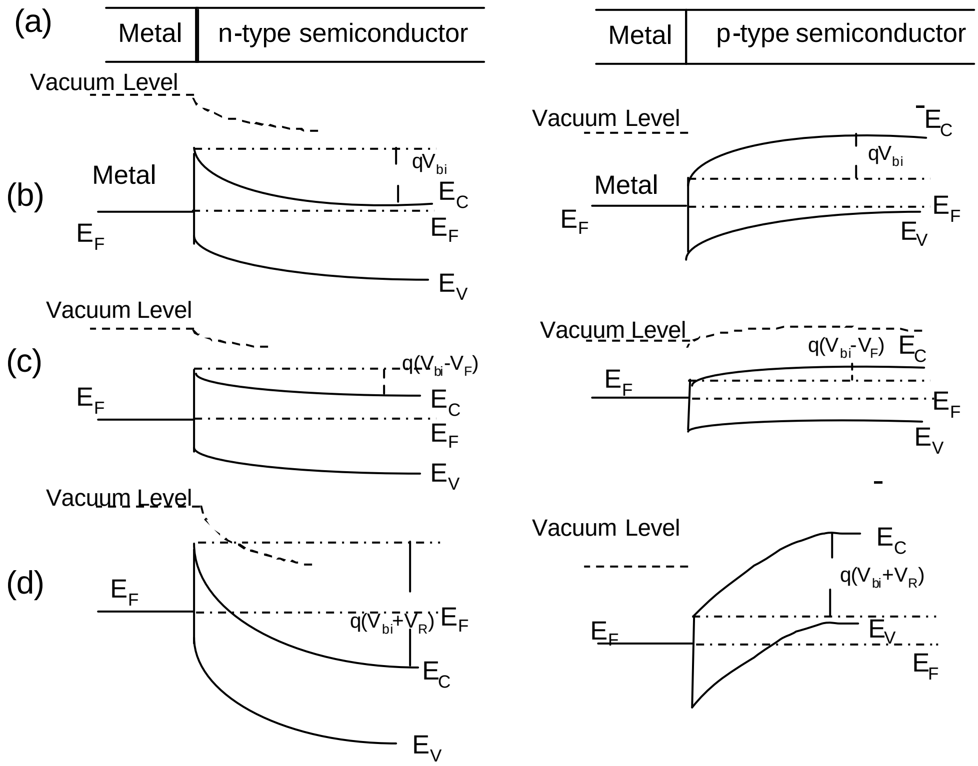

Figure 4.2. Energy diagrams of (a) n-type and p-type semiconductors in contact with metal, (b) in thermal equilibrium, (c) forward biased, (d) reverse biased conditions

4.1. The Schottky Junction

The Schottky effect is the image-force-induced lowering of the potential energy for charge carrier emission when an electric field is applied. In order to see this effect, consider a metal-vacuum system first. For an electron to escape to vacuum from an initial energy at Fermi level, the work function q? m defines the minimum energy required. Figure 4.3 illustrates the energy band diagram between a metal surface and a vacuum. When an electron is present at a distance of x from the surface of the metal, there will be a positive induced charge on the metal located at –x from metal's surface and thus negating the electrical potential on the metal's surface. This positive charge is called the image charge, and the force it exerts is called the image force [45].

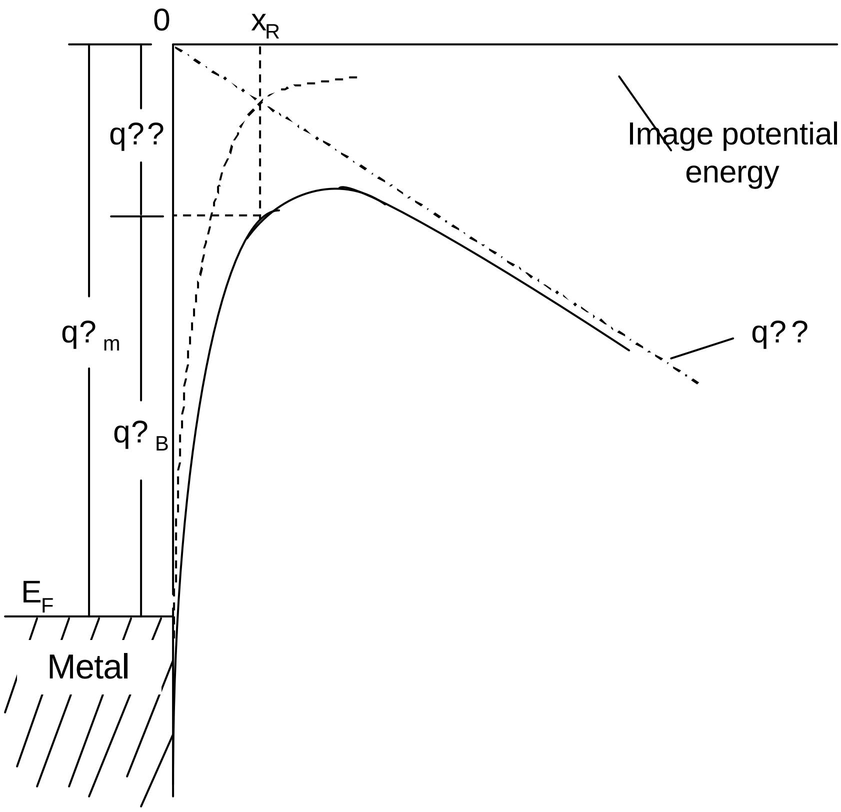

Figure 4.3. Energy band diagram between metal and vacuum. q? m is the metal work function. The effective work function is lowered when an electric field is applied

Replacing the external field with the maximum field at the interface, and free space permittivity ?o is to be replaced with ?s for characterizing the medium; the condition for metal-vacuum condition can also be applied to metal-semiconductor interfaces.

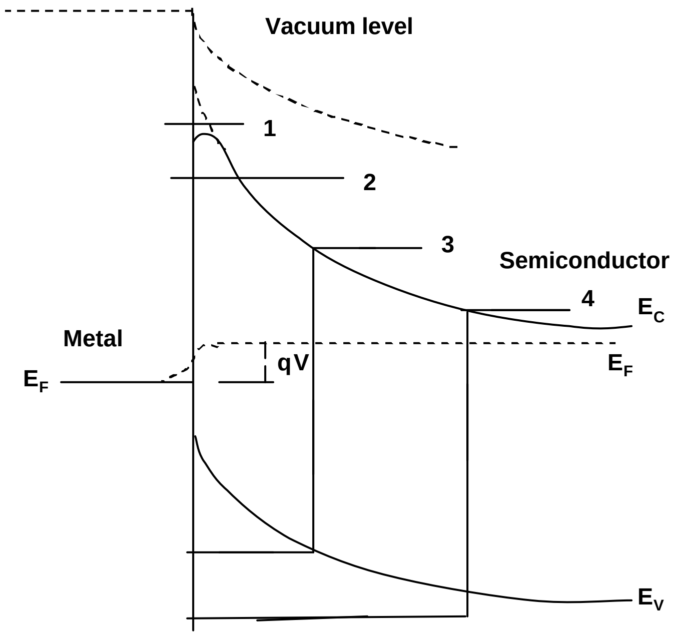

Figure 4.4. The current transportation in a metal-semiconductor contact

The current transport in metal-semiconductor contacts is due mainly to majority carriers, in contrast to p-n junctions, where current transport is due mainly to minority carriers. In figure 4.4, four processes of current transportation in a metal-semiconductor junction is shown. These processes are (1) transport of electrons from the semiconductor over the potential barrier into the metal (the dominant process for Schottky diodes with moderately doped semiconductors); (2) quantum-mechanical tunneling of electrons through the barrier (important for heavily doped semiconductors and responsible for most ohmic contacts); (3) recombination in the space-charge region (identical to the recombination process in a p-n junction) ; and (4) hole injection from the metal to the semiconductor (equivalent to recombination in the neutral region). In addition to these processes, there can be edge leakage current due to a high electric field at the periphery of contact, or interface current due to traps at the metal-semiconductor interface.

4.2. Metal-Semiconductor-Metal Configuration

Figure 4.5 shows a diagram of metal-semiconductor-metal junction (MSM). It is basically two Schottky diodes connected back to back [46]. Consider the current transport in a symmetrical MSM structure with a uniformly doped semiconductor. When a sufficiently high electric field is applied, the field will reach through the device. The corresponding band diagram is shown in figure 4.6. Under this condition, thermionic injection of holes across the barrier occurs. The injected holes can traverse the drift region. There will be a time delay called transit time delay in reaching the metal contact, corresponding to the time of holes reaching to the contact [45].

For a small positive voltage applied to contact 1 with respect to contact 2 (contact 1 is forward-biased and contact 2 is reverse-biased). The depletion layer width's are:

$$W_1 = \sqrt{\frac{2e_s}{qN_A}(V_{bi} - V_1)} \tag{4.4}$$

$$W_2 = \sqrt{\frac{2e_s}{qN_A}(V_{bi} + V_2)} \tag{4.5}$$

Where W_1 and W_2 are the depletion layer widths in the junction in the p-layer for the forward and reverse-biased barriers, respectively; N_A is the acceptor ionized impurity density; and V_{bi} is the built in voltage. The current in this configuration, is the sum of the reverse saturation current, generation-recombination current, and surface leakage current.

As the voltage increases, the reverse-biased depletion region will eventually reach through to the forward-biased depletion region. The corresponding voltage is called the reach-through voltage V_{RT}. Figure 4.6 shows the field distribution of an MSM configuration at reach through. If the voltage is increased further, the energy band at contact 1 can become flat. In the flat-band condition, the field is zero at x=0 when V_{bi}= V_1. The corresponding voltage:

$$V_{FB} = \frac{qN_A W^2}{2e_s} \tag{4.6}$$

This is defined as the flat band voltage. The relation between the applied voltage and the barrier height is:

$$V_{bi} - V_1 = \frac{(\mathrm{V_{FB}} - V)^2}{4\mathrm{V_{FB}}} \tag{4.7}$$

The reach-through point x_R as shown in figure 4.6-a is given by:

$$X_R / W = \frac{(\mathrm{V_{FB}} - V)}{2\mathrm{V_{FB}}} \tag{4.8}$$

After reach through, the hole current thermionically emitted over the hole barrier ? $_{Bp}$ becomes the dominant current:

$$Jp = A_p^* T^2 e^{-q(?\,Bp+Vbi)/kT} (e^{qV1/kT} - 1) \tag{4.9}$$

where A_p^* is the effective Richardson constant. Note that the current density increases exponentially with the applied electrical potential.

(a)

(b)

(c)

(d)

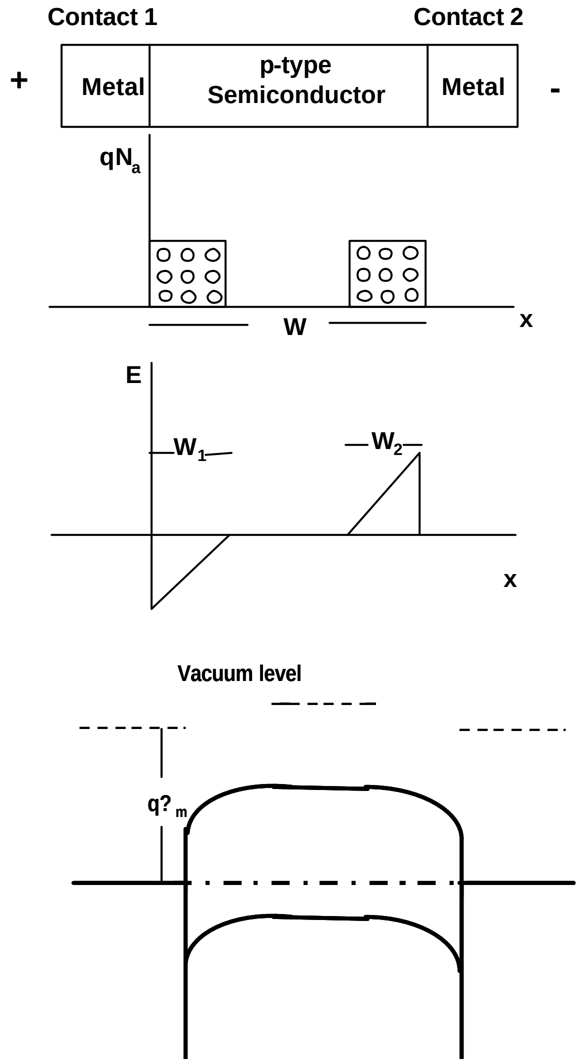

Figure 4.5. a) Schematic of MSM contact, b) the expected carrier distribution, c) the electric field distribution, and d) the unbiased band diagram

(a)

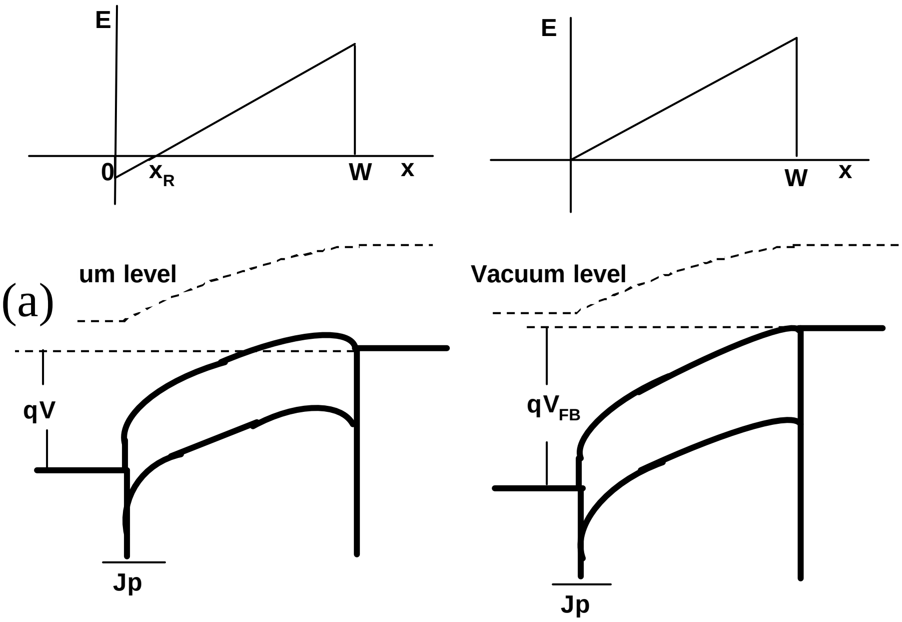

(b)

Figure 4.6. The electric field distribution and band diagram of MSM contact at a) reach through and b) flatband configuration

4.3. Ohmic Contact

In the metal-semiconductor junction, if there is a negligible contact resistance, the contact is called Ohmic contact. It is a junction between a metal and semiconductor where the contact does not limit the flow of the current [47]. The current is only limited by the resistance of the semiconductor outside the contact region. Figure 4.7 shows the band diagram of an Ohmic contact before and after it is established. The electrons in the figure, tunnel into the semiconductor and pile in the conduction band near the junction. The equilibrium is reached when the electrons in the junction prevent further electron accumulation.

The semiconductor region near the junction is called the accumulation region. The electrons passing from metal to the semiconductor pile up in this region. Going from the far end of the metal, to the far end of the semiconductor, there are always conduction electrons in the Ohmic contact, whereas, in Schottky junction, the conduction electrons in metal are separated from those of the semiconductor [47].

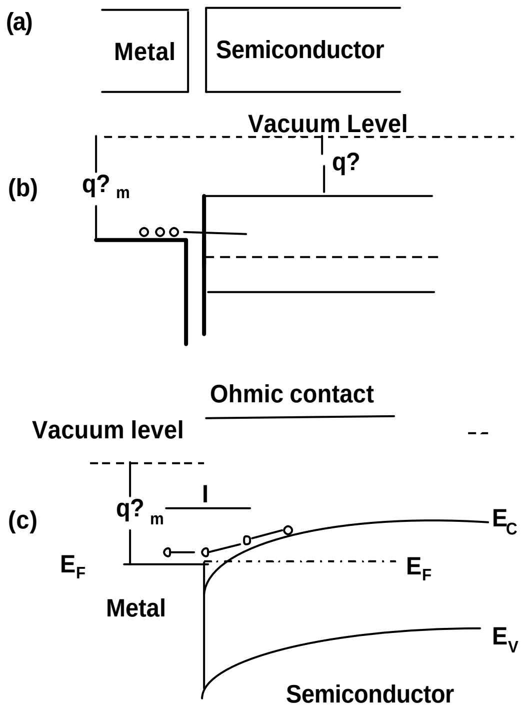

Figure 4.7. a) One dimensional structure of a metal-semiconductor before contact, and their band diagrams forming an ohmic contact b) before c) after the contact is established

Excess electrons in the junction increase the conductivity of the semiconductor. The bulk of the semiconductor has higher resistance than that of the contact. Therefore, when an electrical potential is applied to the metal-semiconductor structure, the higher voltage drop is observed at the bulk of the semiconductor. The current is determined by the resistance of the bulk semiconductor.

4.4. Electrical Input

As explained in chapter 3, silicon's optical characteristics can be changed by an electrical input. By placing two probes to the poles of the sphere, we made the metal-silicon-metal (MSM) contact. Figure 4.8 shows the schematic diagram of the MSM contact that was used in our experiments, whereas figure 4.9 shows the pictures of the contact of metal probes and sphere.

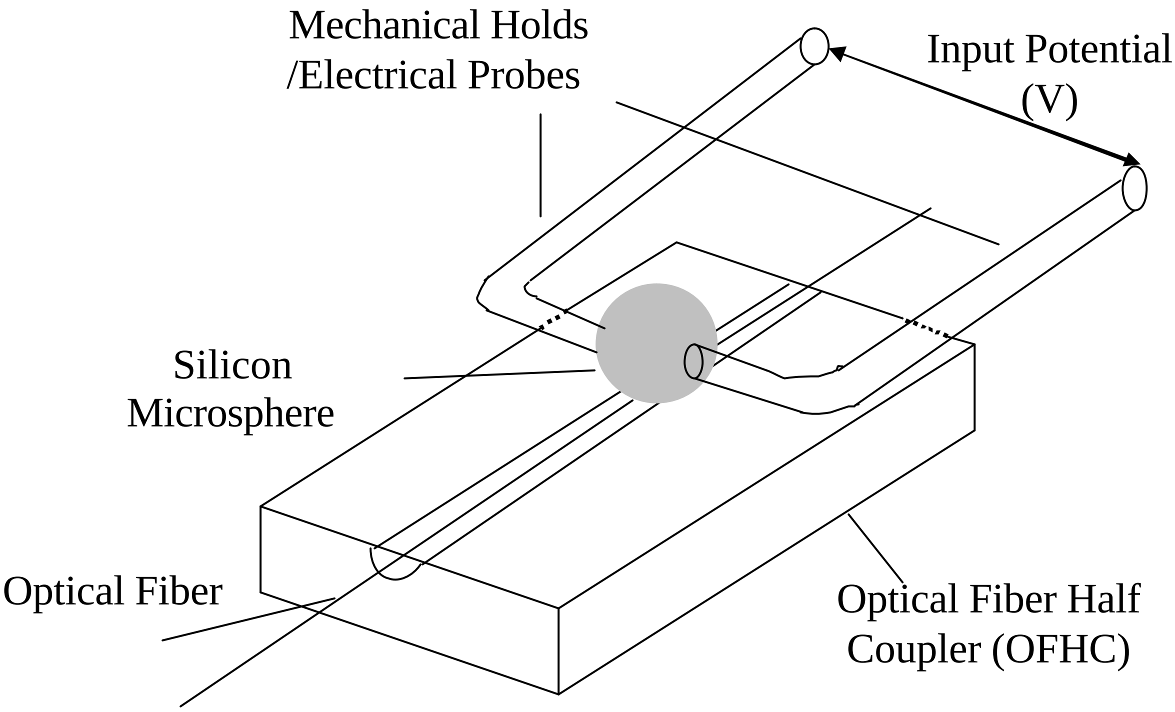

Figure 4.8. The schematic of the electrical input and the microsphere over the OFHC

The probes we used are brass probes that are connected to the electrical circuit given in figure 4.10. The output of the circuit gives a DC ranging between ±9V. This circuit was used in the early stages of the experiment, whereas, later on the 9V batteries were changed with 65 Volt batteries and the switch was taken off. The diagram for the updated electrical circuit is given in figure 4.11.

The alignment of the probes and the sphere was significantly important, for that was determining the contact with the metal and the semiconductor. For different metal-silicon contacts, we obtained different current (I) and potential (V) characteristics. Figure 4.12 shows an earlier graph of I-V characteristics of the MSM structure that was obtained in our experiments.

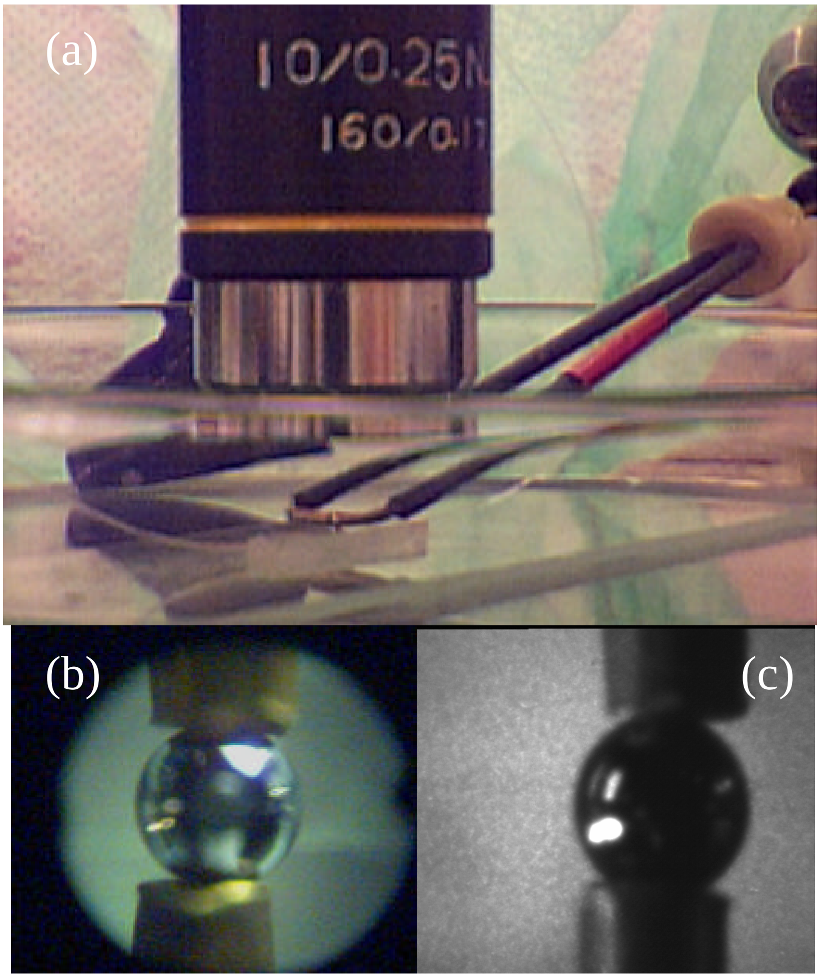

Figure 4.9. Picture of metal probes and silicon contact: a) Side view of the OFHC and metal probes holding the microsphere b) Top view of the metal probes holding the sphere from the poles c) Top view of the metal probes holding the sphere from the poles taken by an IR camera

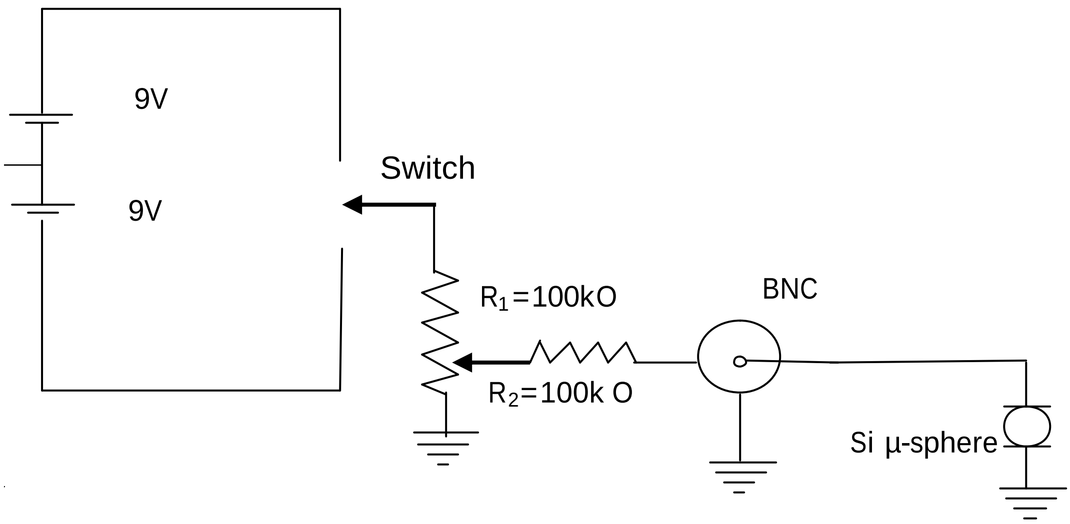

Figure 4.10. The diagram of the electrical circuit of the experimental setup for the electrical input

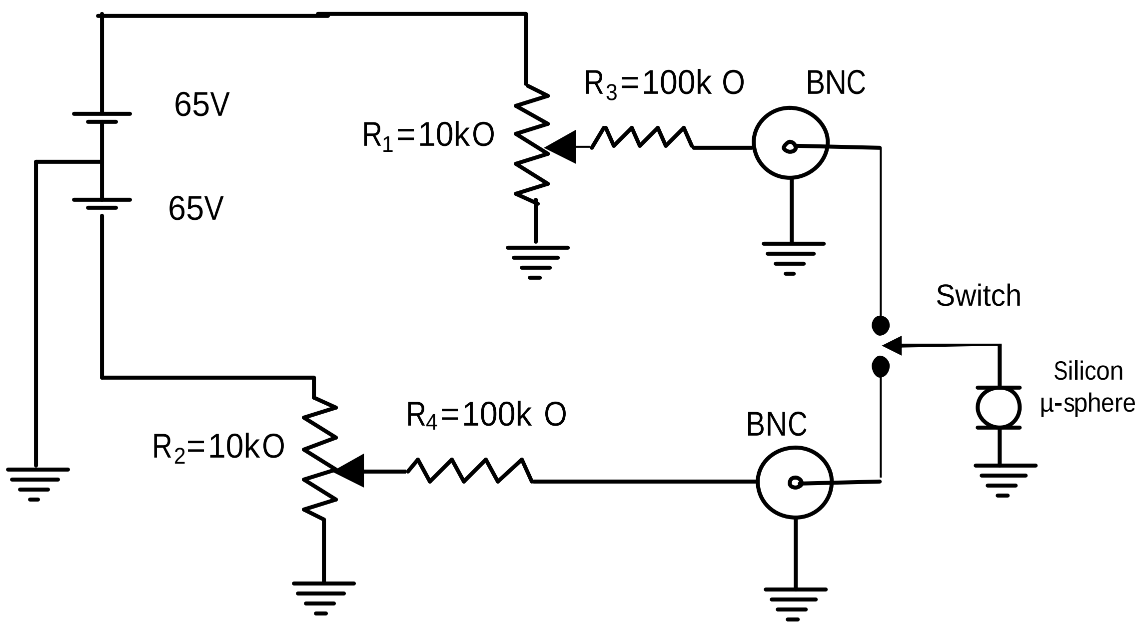

Figure 4.11. The diagram of the updated electrical circuit of the experimental setup for electrical input

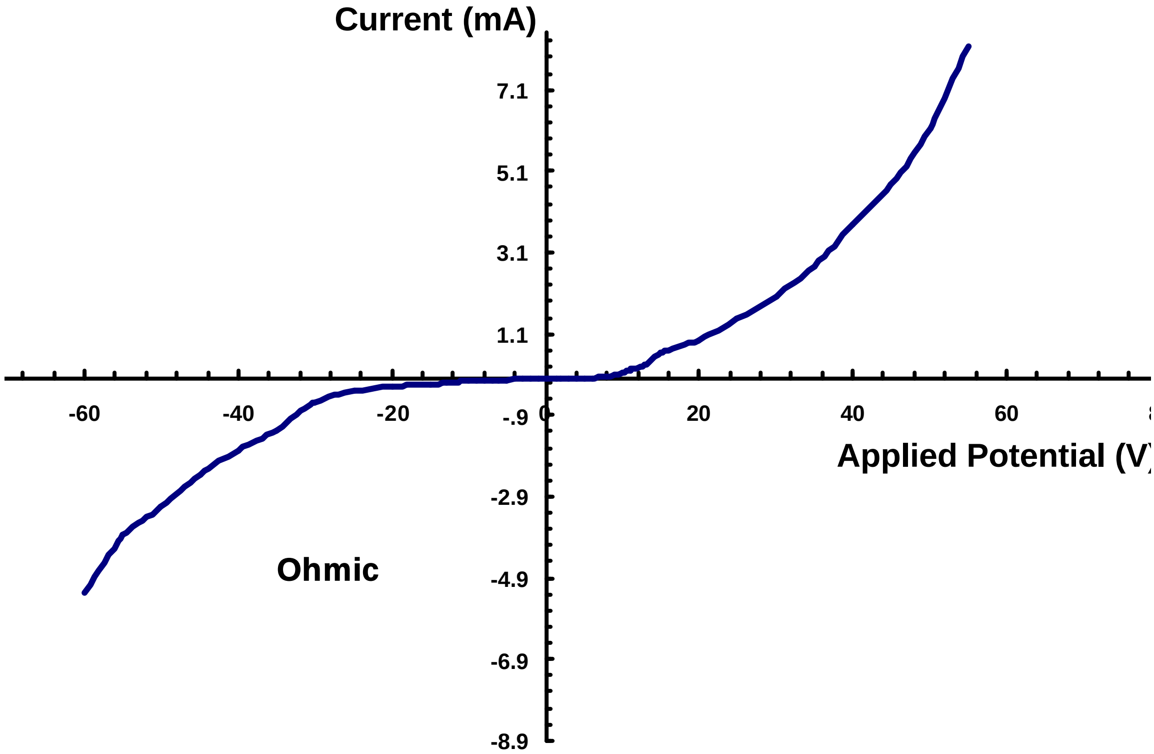

Figure 4.12. a) The I-V characteristics of the experimental metal-silicon-metal (MSM) contact

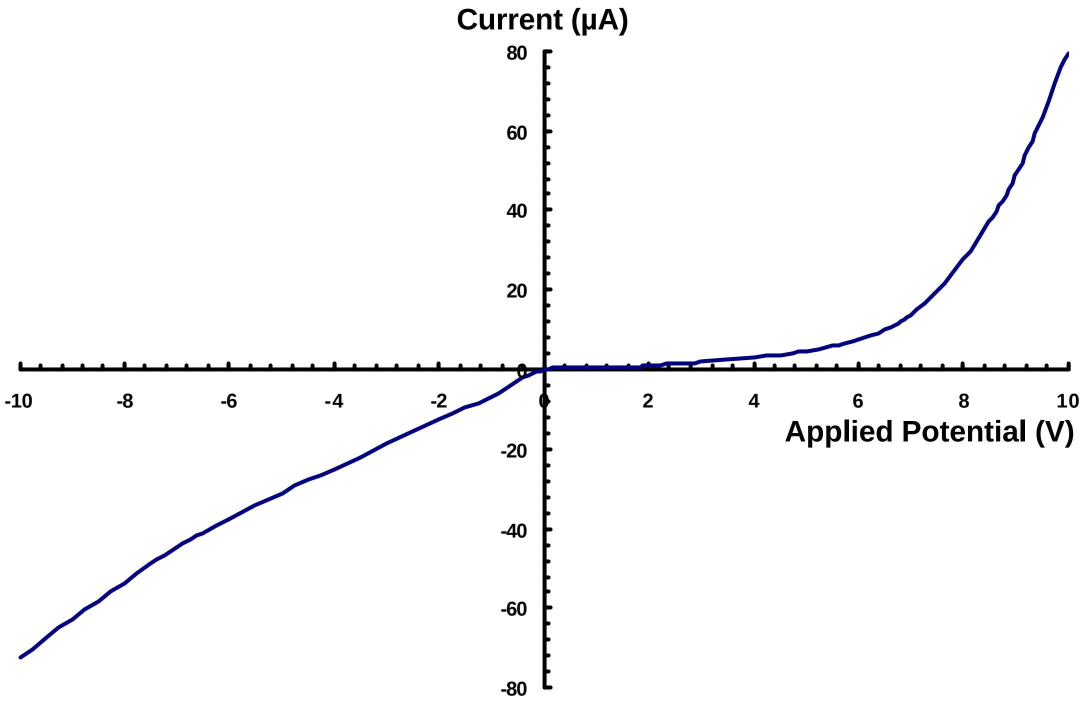

Figure 4.12. b) The expanded I-V characteristics of the experimental metal-silicon-metal (MSM) contact

The I-V characteristics illustrated in figure 4.12 support that the diode is two Schottky diodes connected back to back. The graph is not fully symmetric, due to the non-symmetric contact. The contact resistance differences are not significant, since contacts are both Schottky contacts.

Figure 4.12 is not the only current-voltage characteristics that were obtained from the contact. As mentioned earlier, different contacts in the MSM structures resulted in different current-potential relations. After taking the I-V characteristics of figure 4.11, the sphere's position is changed and the MSM structure was formed anew. The new MSM structure's electrical I-V characteristics are shown in figure 4.13.

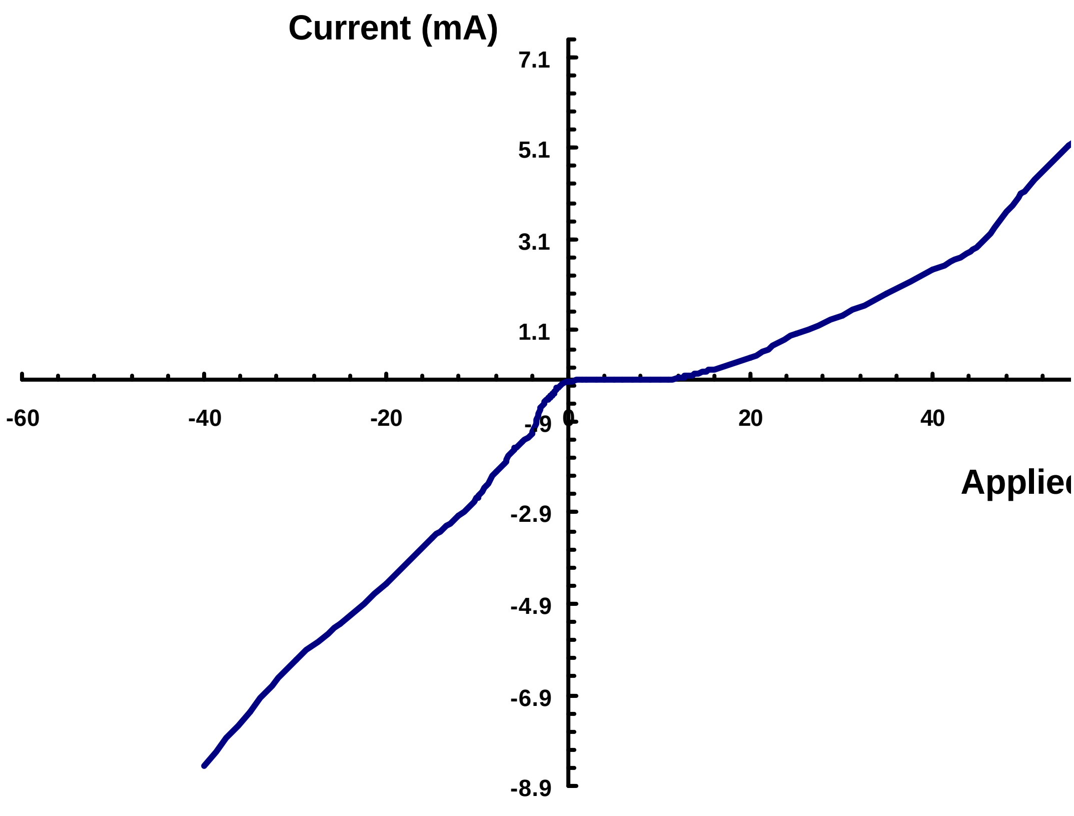

Figure 4.13. a) The I-V characteristics of the experimental metal-silicon-metal (MSM) contact

The significance of figure 4.13 is that, it is not symmetric. The forward biased current seems to depend on the potential exponentially, whereas the reverse-bias current seems to depend on the potential nearly linearly. It is possible in the configuration that the contact 2 made a negligible resistance at the contact and thus the reverse-bias current-voltage relation turned out to be Ohmic contact.

(i)

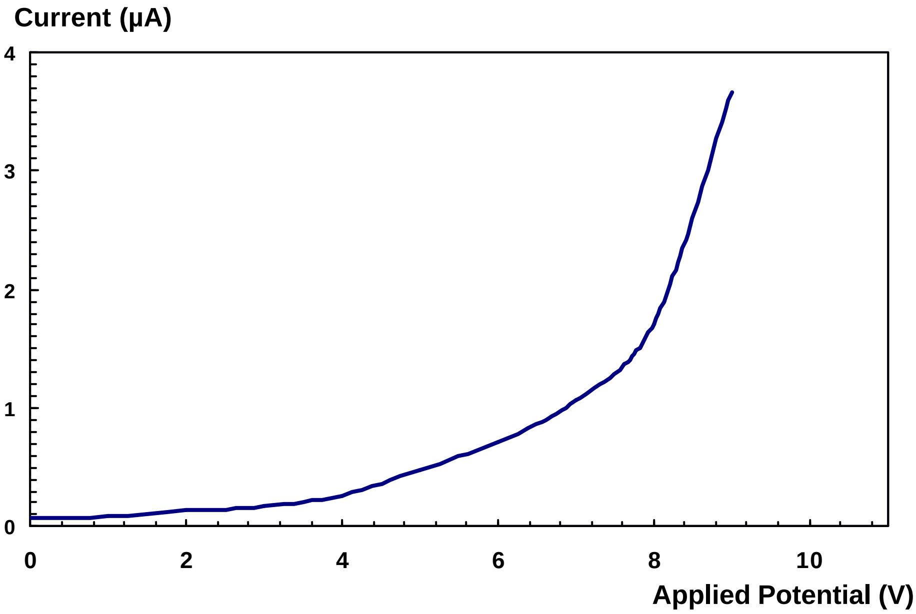

(ii)

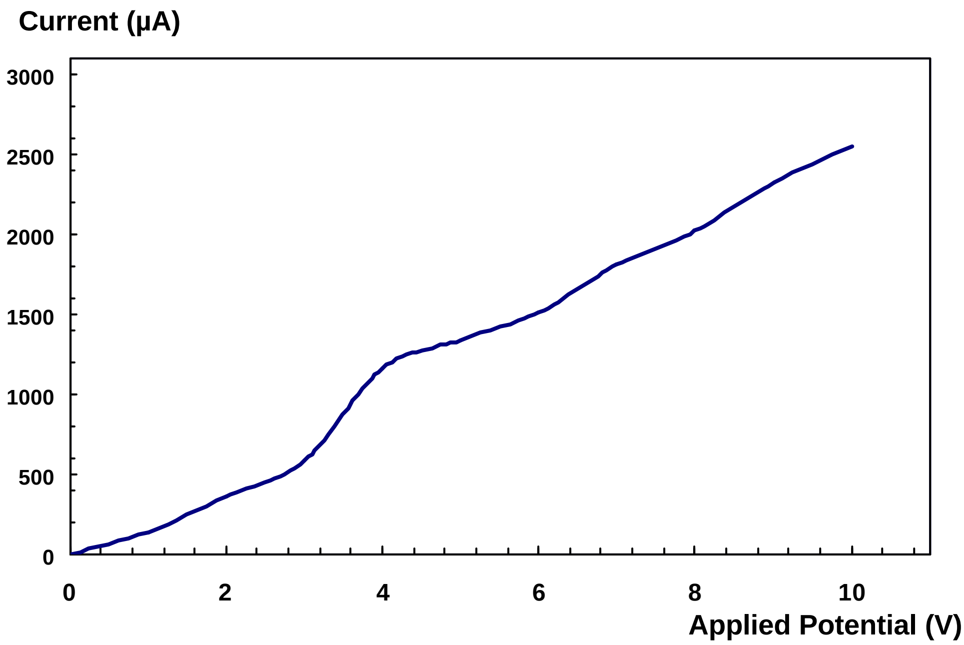

Figure 4.13. b) The I-V characteristics of the experimental metal-silicon-metal (MSM) contact, (i) positive applied potential, (ii) negative applied potential

5. ELASTIC LIGHT SCATTERING FROM A SILICON MICROSPHERE

The schematic of the experimental setup is shown in figure 5.1. A tunable distributed feedback (DFB) semiconductor laser with a center of wavelength of 1475.5 nm is used to excite the MDR's of the microsphere. Wavelength tuning is achieved by tuning the temperature of the DFB Laser with a laser diode controller (LDC). Laser light is coupled to into the optical fiber half coupler (OFHC) by lenses. The optical fiber used in the OFHC is a standard 1500 nm single-mode fiber.

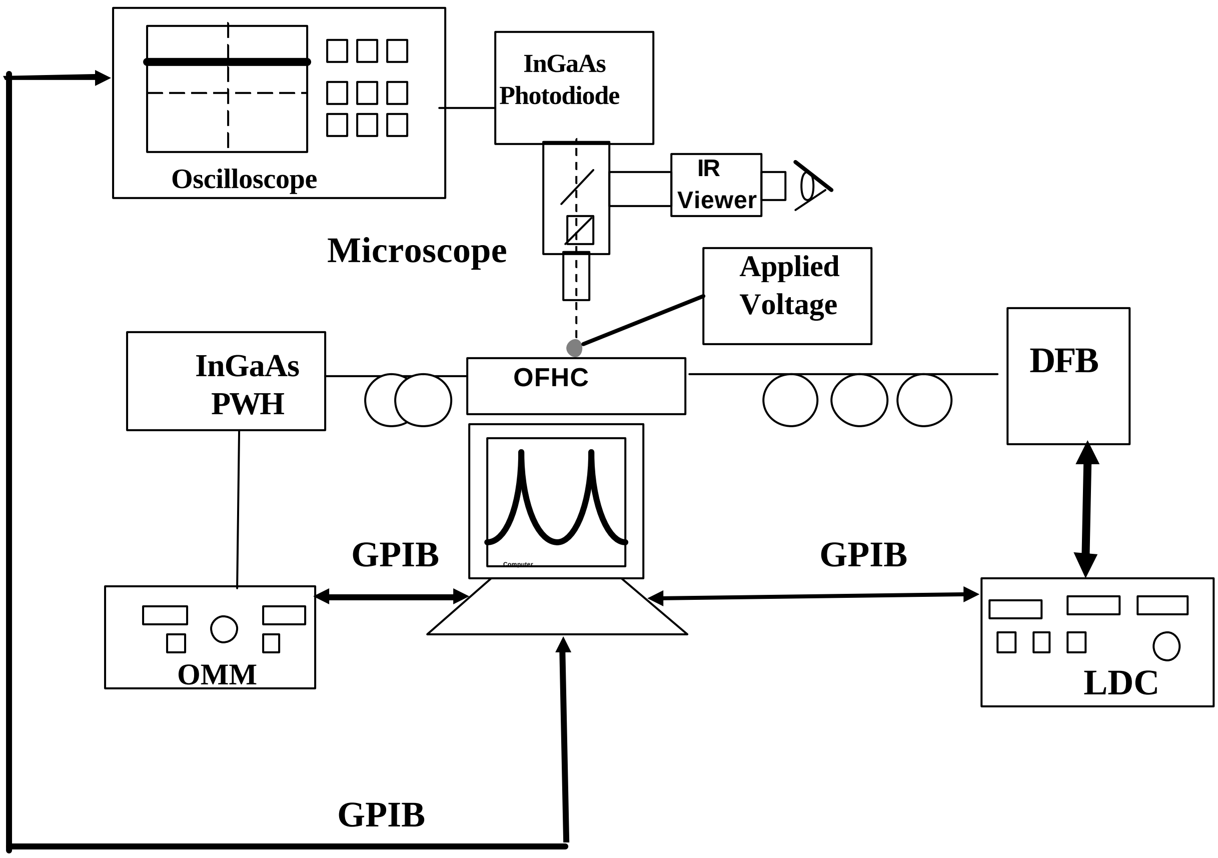

Figure 5.1. Schematic of the experimental setup for observing the MDR's of silicon microsphere , and the resonance shifts with the applied electrical potential

The transmitted light through the optical fiber is measured by an optical multimeter (OMM) with InGaAs Power/Wave Head (PWH). The scattered light from the microsphere is collected by a microscope lens is measured by an InGaAs photodiode. The InGaAs photodiode signal is sent to the digital oscilloscope for signal monitoring and data acquisition. Data acquisition and control are performed with IEEE-488 GPIB interface and the Labview program which was written previously by Senol Isçi and updated by Ulas Kemal Ayaz.

5.1. Coupling Light into MDR's of Microspheres

A significant challenge in utilizing high-Q narrow-linewidth optical resonators is the need to excite resonant modes efficiently while, simultaneously, making sure that the Q is not compromised. In the case of the microsphere, this implies that along with maintaining a sphere surface clean from surface imperfections and particles that would attenuate or scatter light out of the resonant modes, the external factors to affect Q must be controlled [48]. A significant element here is the coupler, which passes the light into and out of the microsphere.

The ideal microsphere MDR coupling device should have the characteristics of a) performance of efficiently exciting MDRs; b) alignment of sphere to couple; c) clearly defined ports; d) integrable and robust structure; and finally e) a low cost and consistant fabrication process [49].

There are a variety of evanescent field techniques to coupling to MDR's of microspheres efficiently. These techniques range from bulk prisms to OFHCs [50], examples of which you can see in Figure 5.2. For these techniques, it is required that at the coupler's glass-air interface, the energy transfer from the coupler to the microsphere's whispering gallery modes is an optical field that decays exponentially.

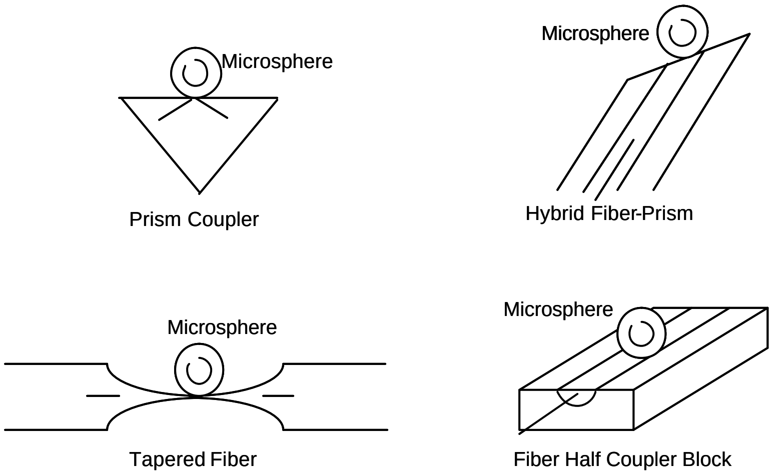

Figure 5.2. Evanescent wave coupling techniques. Source: Laine [50]

The overlap of the sphere and the coupler mode fields and the matching mode propagation constants are the primary factors that determine the efficiency of an evanescent coupler. Yet, there are other factors that might play a significant role in the efficiency of the coupler, such as the length of the coupler, and how steep the fiber is curled inside of the coupler [51]. Ease of alignment and the clearly defined ports narrow the field of evanescent-field couplers to purely guided wave devices. For instance, in bulk prisms, the positions of all components (such as light source, prism, and sphere) must be carefully adjusted in order to reach the optimal coupling region conditions. In addition, the MDR's of the sphere can be observed by either collecting the elastically scattered beam or collecting the light from the prism; whereas there is no need for elaborate spatial position optimization when a tapered-fiber guided wave coupler is used.

5.1.1. Optical Fiber Half Coupler

The optical fiber half coupler (OFHC) is made of an optical fiber buried in glass block. In order to be able to get access to the optical mode in the fiber, the fiber is polished very close (1 μm) to the core. Placing a microsphere on the exposed surface near the evanescent field of the fiber optic core will cause an energy exchange between the waveguide mode of the fiber and the MDR of the sphere [52]. The optical fiber buried into the glass substrate to make OFHC is 1500 nm single-mode fiber with a core radius of 9 µm with refractive index of 1.47, and a cladding with index of refraction of 1.45, and a radius of 62.5 µm.

5.1.2. MDR Excitation for the Microsphere

In order to use microspheres in applications, efficient light coupling into the sphere is required. Two basic methods of illumination in applications of microspheres are plane-wave and Gaussian beam illumination.

In plane wave illumination, the density of the incoming beam is uniformly distributed. Figure 5.3 shows an example of the plane wave coupling into the microsphere. The lines inside the sphere are the optical paths within the cavity, arrows pointing the direction of the beams. As can be seen in the figure, the internal intensity of the resonator is mainly focused on the front and the rear surfaces of the microsphere.

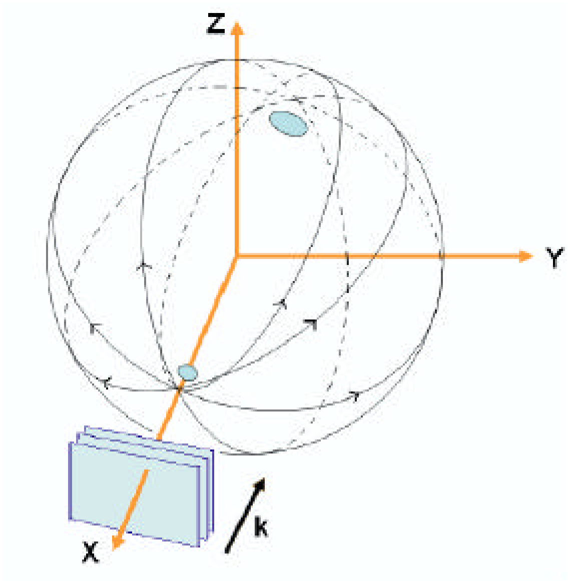

Figure 5.3. The expected optical paths inside the microsphere for plane wave illumination

In Gaussian beam excitation, the efficiency of the excitation of MDRs depend on the beam's focusing and the position of the beam waist with respect to the sphere. Figure 5.4

gives an illustration of Gaussian beam coupling into a microsphere and elastic scattering angles of the beam.

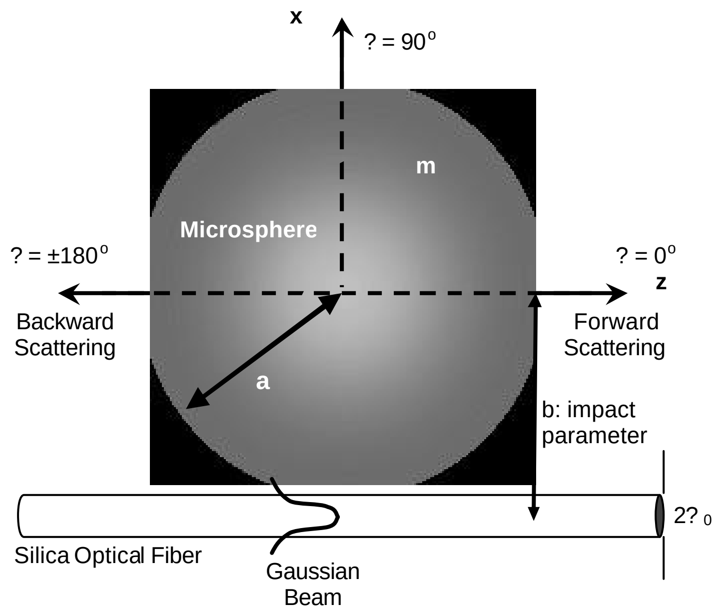

Figure 5.4. Excitation of MDRs by a Gaussian beam illumination

The fiber microsphere system shown in figure 5.4 requires the study of generalized Lorenz-Mie theory. This theory of was implemented as generalization of Lorenz-Mie theory, and then was used to study Gaussian beam scattering of tight beam localization. The model predicts that the efficiency of MDR excitation is particularly high when the beam illuminates the sphere near the edge.

5.2. Experimental Results from Silicon Microsphere

Morphology dependent resonances (MDR's) of silicon microspheres are excited by a tunable continuous wave DFB laser with a central wavelength of 1475 nm. Efficient coupling to MDR's is achieved by using an optical fiber half coupler (OFHC) and resonance peaks in the elastic scattering spectra are experimentally observed.

5.2.1. Observing MDR's from a Silicon Microsphere

Silicon microsphere of 500 micrometer is placed over the OFHC, and two metal probes held the sphere in position. Elastic scattering data from the microsphere at 90^0 was collected by using an InGaAs photodetector. Figure 5.5 shows one of the earliest elastic scattering spectra when the coupling between the microsphere and the OFHC is not efficiently coupled.

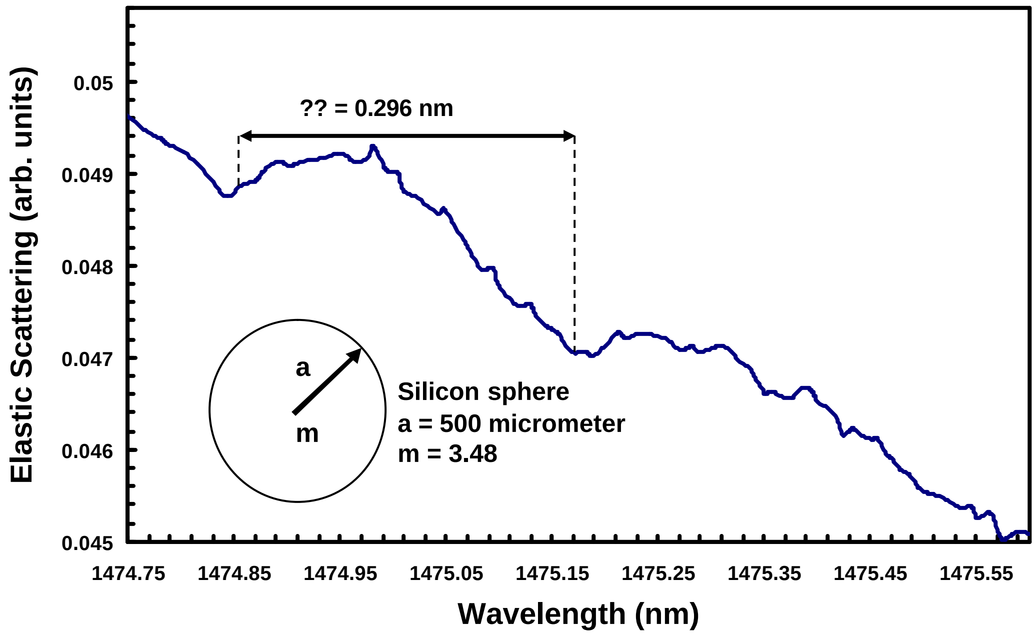

Figure 5.5. Elastic scattering intensity of silicon microsphere with respect to the wavelength

The DFB laser was tuned with a laser diode controller (LDC) by changing the temperature. The temperature range was from 19 ^{0}C to 22 ^{0}C. The mode spacing was measured to be 0.296 nm which is very close to the expected value of 0.293 nm.

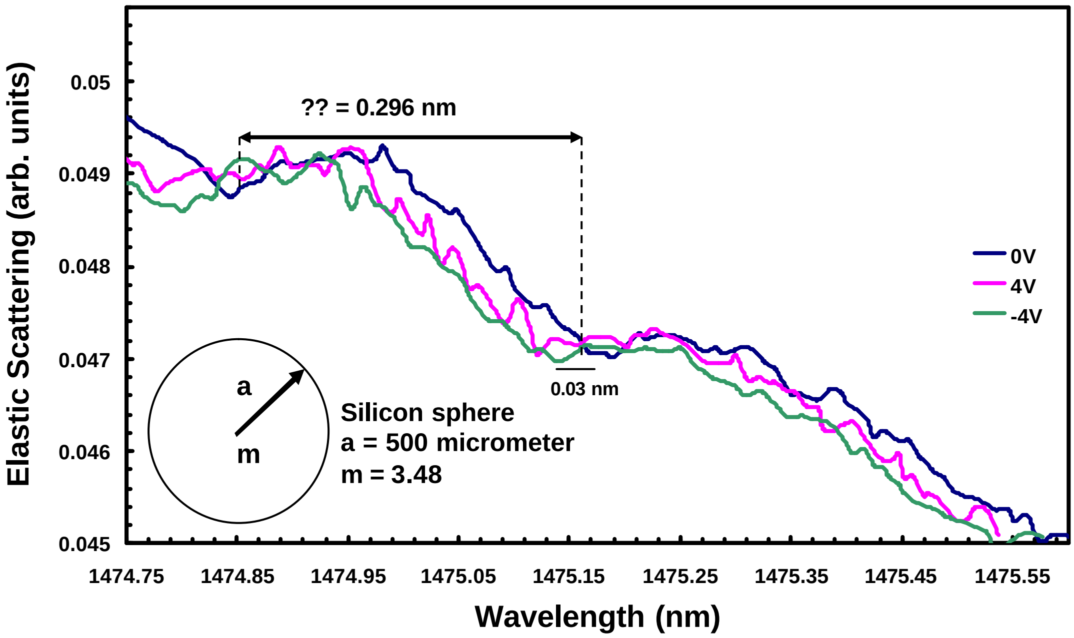

Figure 5.6. Elastic scattering spectrum of silicon microsphere with respect to the wavelength. When the electrical potential is applied, the signal experiences a blue shift.

After the data was taken, electric potential of ±4V is applied to the poles of the microsphere, and the elastic scattering spectra are taken. Comparison of elastic scattering intensities with and without applied potential is given in figure 5.6. The shift of resonant wavelengths is measured to be 0.03 nm for 4 volts of applied electrical potential.

In order to couple the light into the microsphere more efficiently, the sphere was moved over the OFHC. Also the alignment of the photodiode iss changed before taking the spectrum. The temperature range is changed to 19 ^{0}C - 25 ^{0}C before taking the spectrum. Because of the change in the alignment, the intensity of the scattered signal dropped from its previous value. Still the repetitive pattern of the resonance can be seen in the spectrum. After taking the data, discrete potentials ranging from 0V to -3V were applied to the sphere and the intensity of elastic scattering signal was recorded. For all applied potentials, the signal has a blue shift and the value of the shift is proportional to the applied potential.

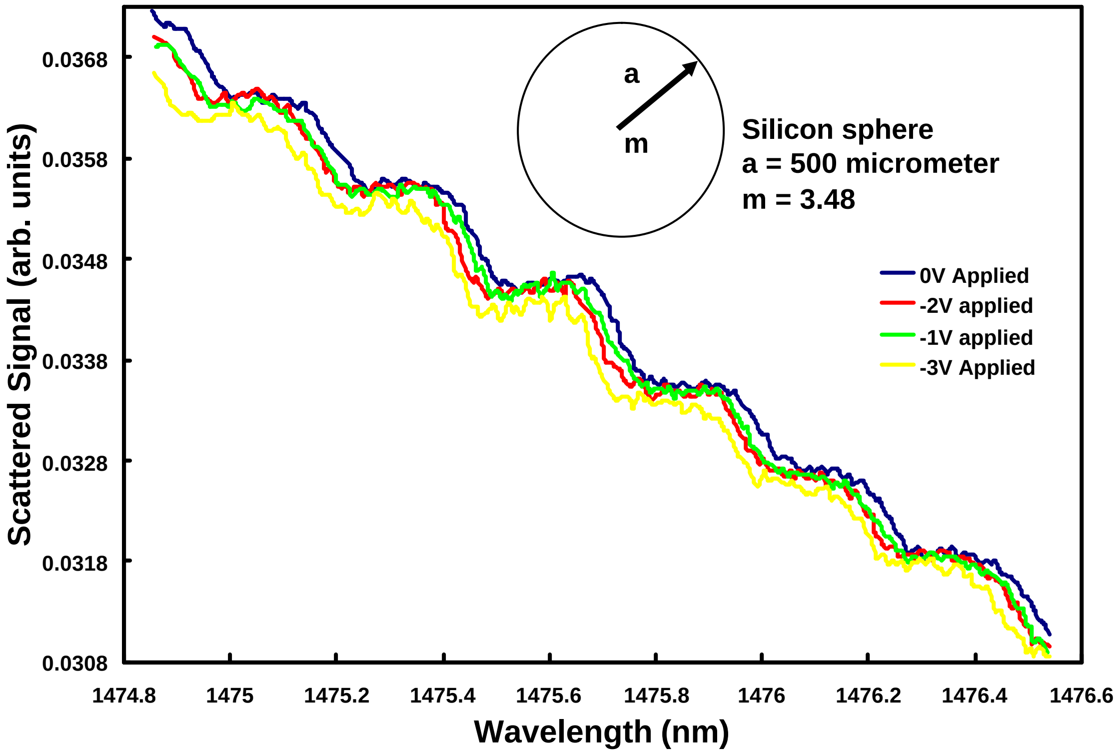

Figure 5.7. Elastic scattering spectra of silicon microsphere

The resonance observed in the signal still does not have sharp and narrow peaks, so the sphere is moved over the OFHC again and the alignment of the InGaAs photodiode is adjusted. While the temperature is changed by LDC from 19 ^{0}C to 25 ^{0}C the elastic spectrum is recorded. In the data, the FSR of the same mode order is recorded to be approximately 0.280 nm. After the spectrum is taken, potential differences of 3, 6, and 9 volts are applied and elastic scattering spectra data are taken. In figure 5.8, the data taken for each applied potential is displayed. Without changing the position of the sphere, elastic scattering spectra are taken for negative potential differences. -3, -6, -9 volts of DC potentials are applied to the poles of the sphere and the scattered signal from the microsphere is recorded. For reference, the scattering spectrum at zero volt potential difference is taken again. The intensities of scattering signal for each electrical input is shown in figure 5.9.

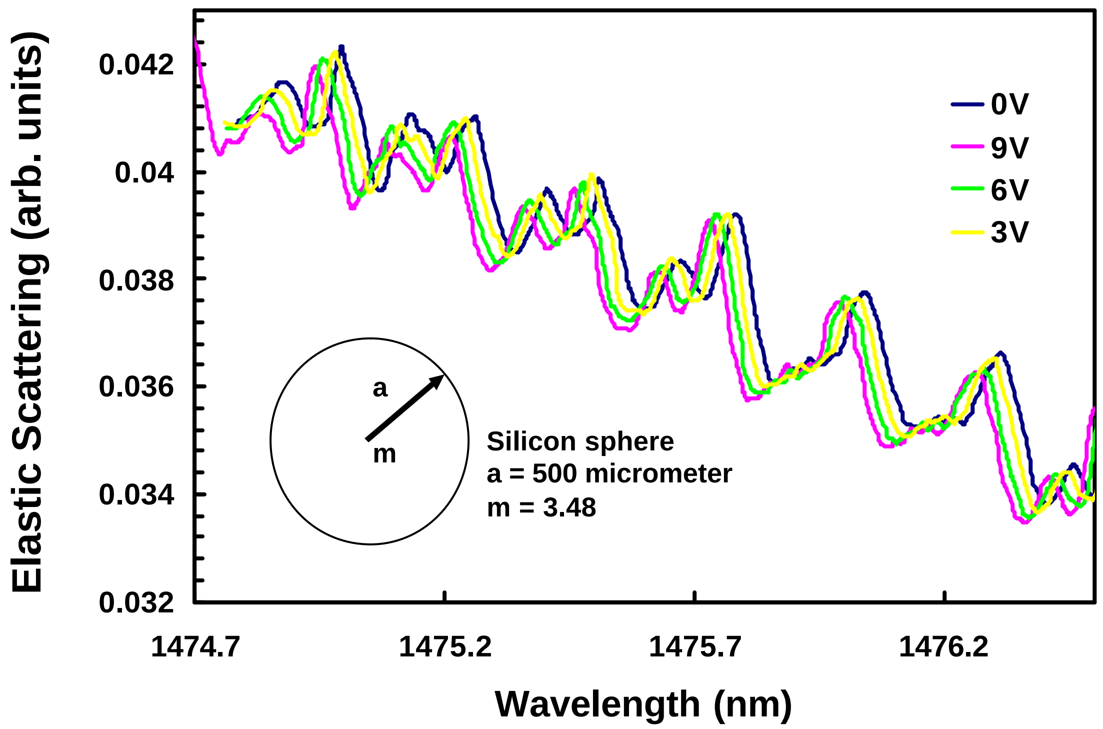

Figure 5.8. The shift in the resonant spectra of the silicon microsphere when positive electrical potential is applied to the sphere

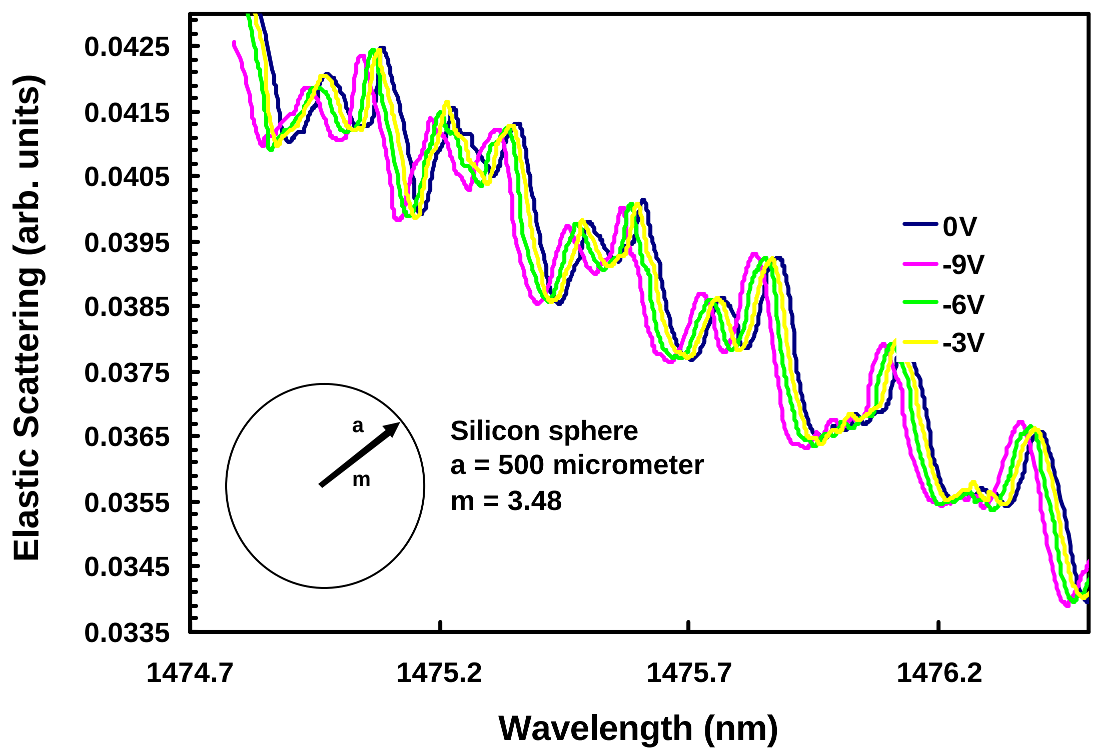

Figure 5.9. The shift in the resonant spectra of the silicon microsphere when negative electrical potential is applied to the sphere

With the applied electrical potential, both for positive and negative voltages, the elastically scattered spectra experienced a blue shift and the shift was proportional to the applied potential difference. From the gathered data, the shifts are ranging from 0.005 nm to nearly 0.05 nm with respect to the applied potential differences.

The data collected, proves that as the applied potential difference increase, so does the shift in the resonance wavelengths. Therefore, applying a higher electrical potential should result in a higher shift in the wavelength. After changing the contact of the metal probes and the alignment of the detector, the elastic scattering spectra are taken once more. Recording the data at zero applied potential, another data is taken for -17 volts of applied potential. More data would be taken, however the sphere's position on OFHC shifted and we did not get the chance to take more data. The spectrum of the elastic scattering for no applied potential as reference and for -17 volt of electrical potential on sphere is given in figure 5.10.

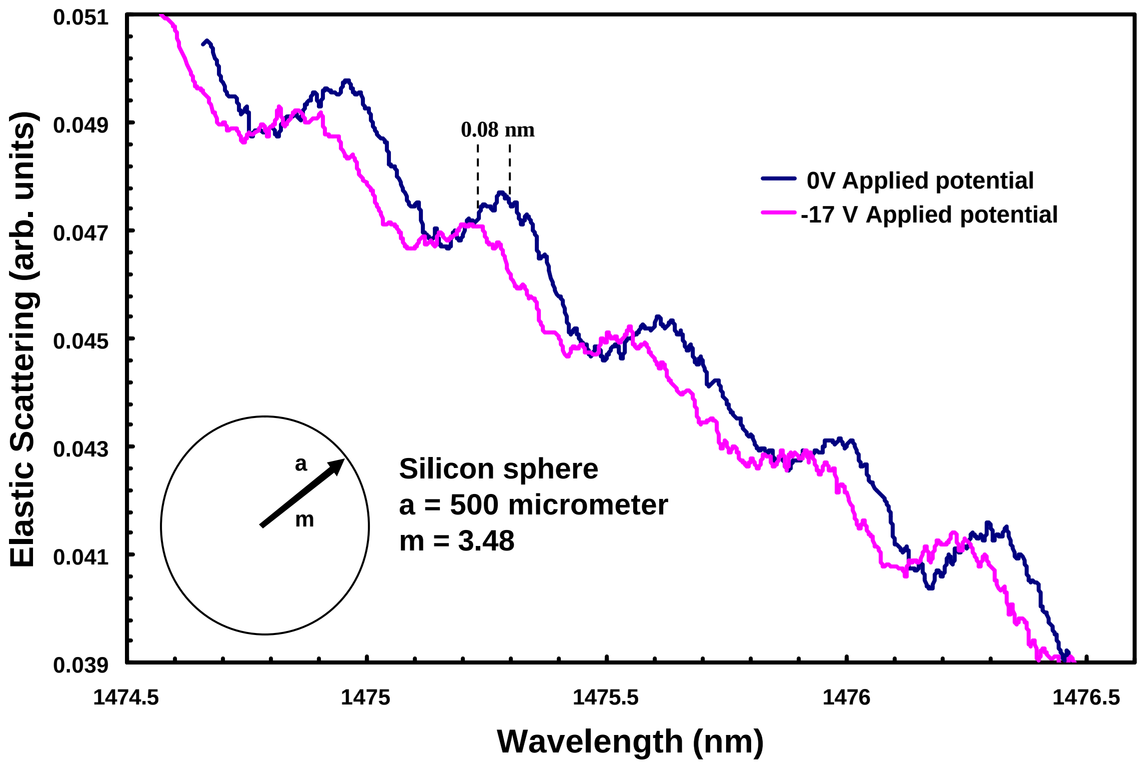

Figure 5.10. The shift in the resonant spectra of the silicon microsphere when a negative electrical potential is applied to the sphere

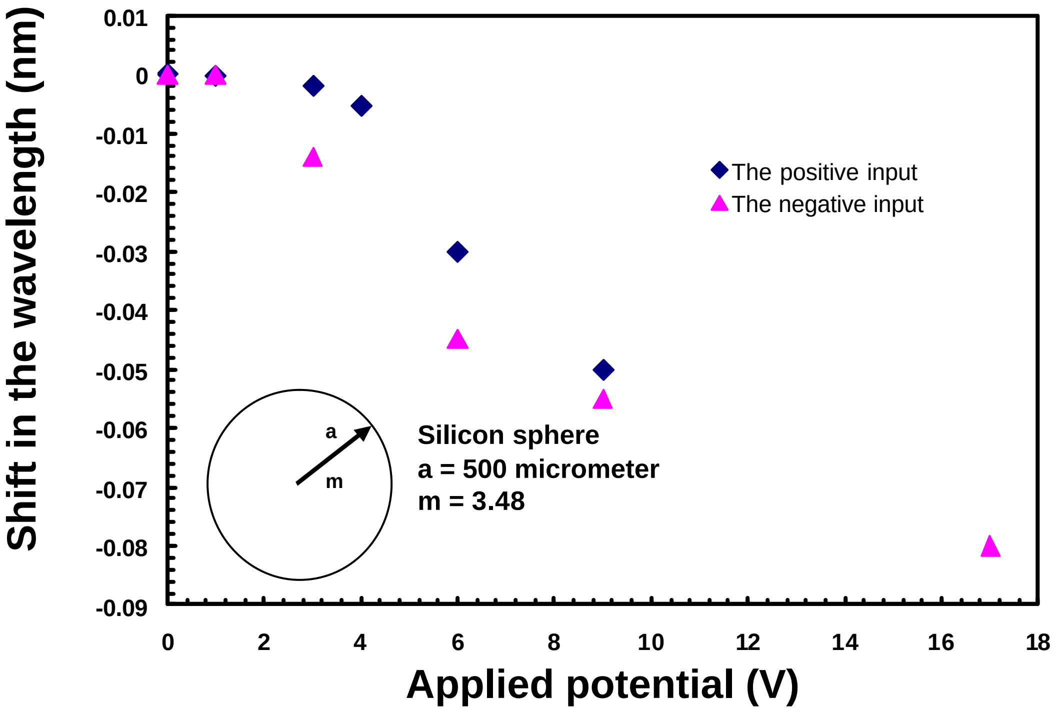

Figure 5.11. The shifts observed in the resonance wavelengths with respect to the applied electric potential

Figure 5.11 summarizes the wavelength shifts observed in our experiments. The positive and negative applied potentials both correspond to negative shifts in the resonance wavelengths. The shifts of the wavelengths were the direct results of the change in the index of refraction. From equation (2.5) for Fabry-Perot resonator and (2.26) for microsphere resonator we can derive the following expression regarding the perturbations in the resonance wavelengths due to the changes in the refractive index:

$$\frac{dm}{m} = \frac{d\,l}{l} \qquad (2.5)$$

Table 5.1. Summary of the observed electro-optic effects on silicon

	Potential Difference(V)	Distance (mm)	E-field (V/m)	?? (nm)	? m (10^{-4})
Koç University	17	1	$17x10^3$	0.08	-1.88
Cornell University	0.94	5×10^{-5}	$15.8x10^6$	0.06	-1.33
Intel Corporation	10	10×10^{-5}	10^9	0.0034	-0.078

Similar experiments with the electro-optic effects on silicon have been studied experimentally by Intel Corporation [53] and Cornell University [54]. Intel Corporation used a Mach-Zender interferometer, applying the electrical input on one branch of the interferometer and measuring the phase difference from the output of the interferometer. Cornell University has used a silicon microring resonator and applied electrical potential on the resonator and observed blue shifts in resonance wavelengths of the transmission spectrum. Table 5.1 summarizes the observation of Intel Corporation, Cornell University, and Koç University. For simplicity only -17 volts, the highest applied electrical potential, has been included in the table.

6. CONCLUSIONS

In this work, after overviewing the Fabry-Perot resonator, MDR's of microspheres are studied. The plane wave Lorenz-Mie theory, and the Gaussian-beam excitations of microspheres are studied. Various optical modulation methods in silicon are demonstrated. Then metal-semiconductor contacts are visited: band diagrams, current-voltage characteristics are provided and the experimental results are presented. Finally experimental results of elastic scattering spectra from a silicon microsphere of 1 mm diameter are presented. The elastic scattered signal from a silicon microsphere is in the near-IR at a wavelength of 1475 nm. The mode spacing ($\Delta\lambda$), i.e. wavelength difference between consecutive mode numbers (n) with the same mode order (l), is measured to be 0.27 nm. Moreover, the effects on electro-optical excitation of silicon have been studied. We have observed blue shifts in the resonant wavelengths of silicon microsphere with respect to the applied potential. This observation heralds novel active optoelectronic silicon devices. Possible wavelength division multiplexing (WDM) applications include optoelectronic devices for filtering, modulation, switching, and detection.

APENDIX: UPDATES TO THE SOFTWARE

A.1. Installing the Software

1. Open "LDC_OMM_TDS_updated.LLB", which is a Labview library file.
2. Select the Ulas_2channels.VI, which is the application software for the LDC 3744B OMM 6810B TDS 210 system.

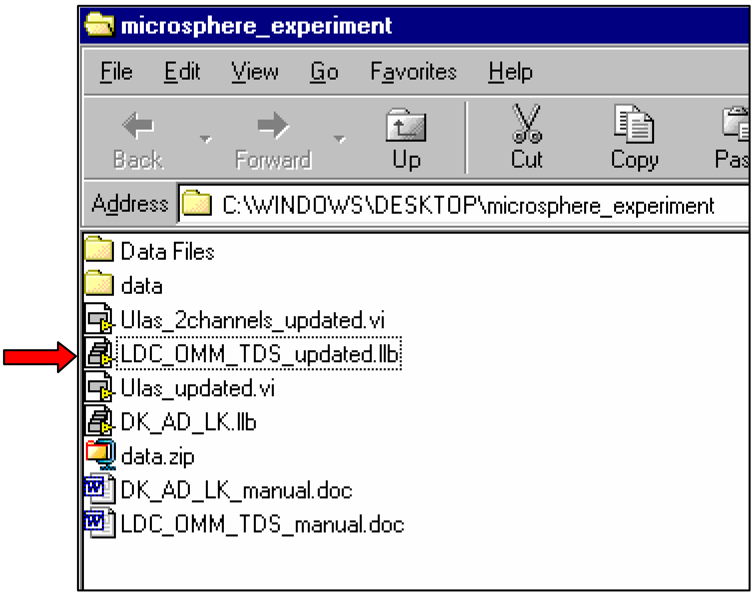

Figure A.1. The labview software files

Once the "Ulas_2channels.VI" has been opened, you are ready to get started.

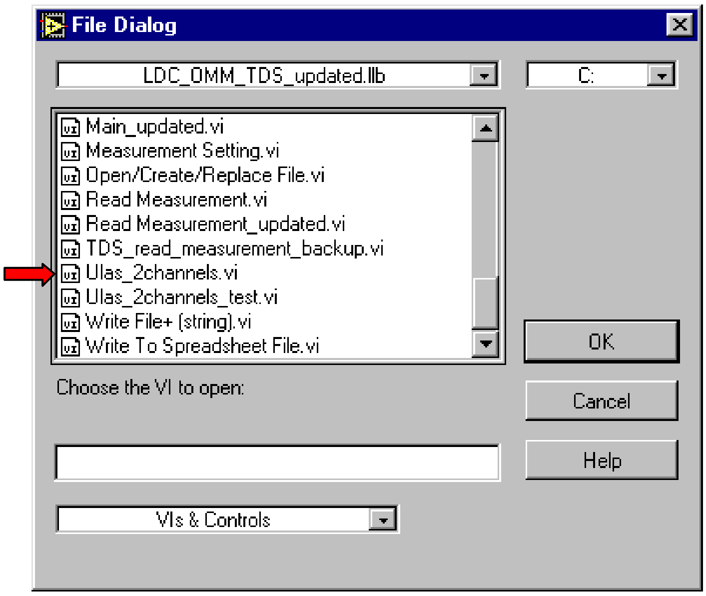

Figure A.2. LDC_OMM_TDS_updated.llb file

A.2. Updates in the user interface

The interface is mainly composed of LDC parameter controls and status displays for various settings of LDC, OMM and TDS. Each graph display the acquired data in the experiment.

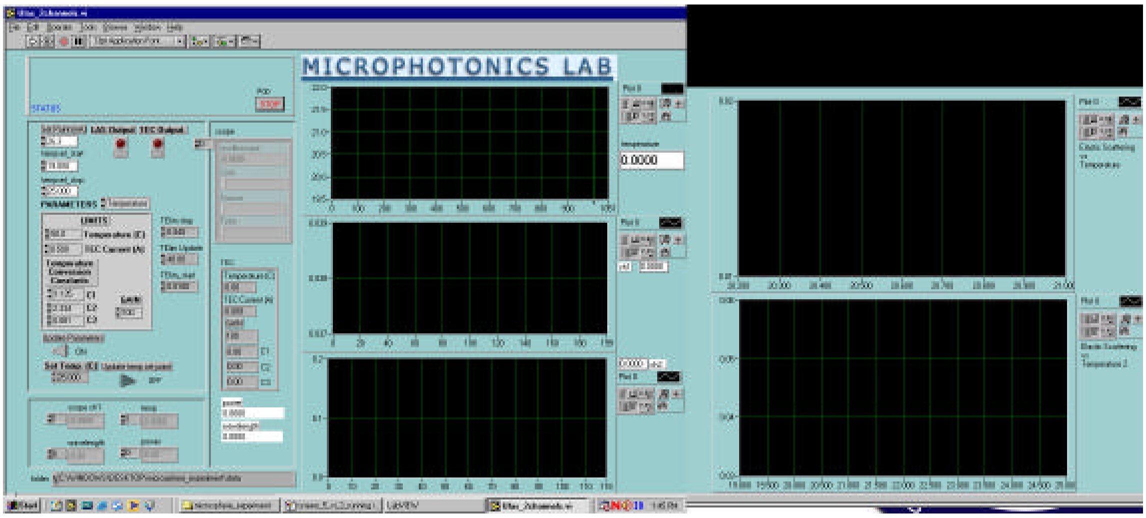

Figure A.3. The user interface of the software

(a)

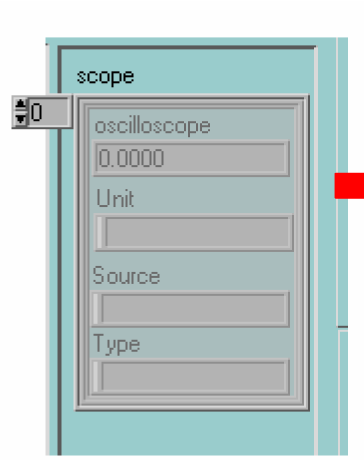

Oscilloscope is data coming from TDS 210. **Unit**, **Source** and **Type** are the parameters set for TDS. When the program is **running** the parameters and the data can be read from the window.

(b)

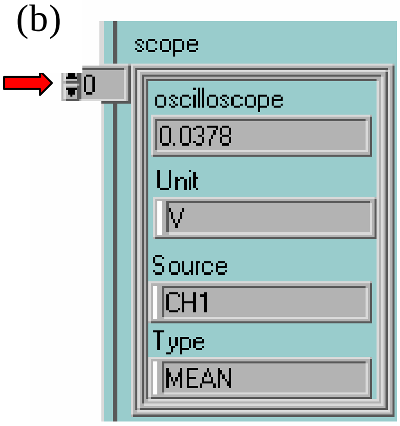

Using the **arrows**, the channel that the data and the parameters read can be changed. When it is "**0**" channel 1 is the **source**. When it is "**1**" channel 2 is the source.

(c)

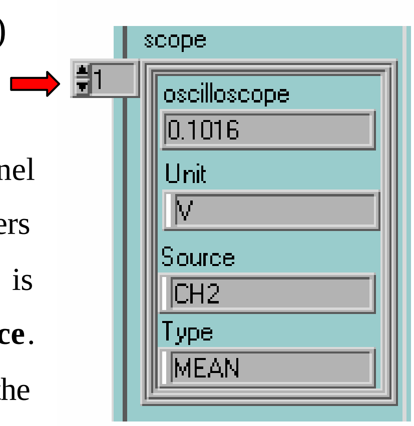

Figure A.4. The data read on the oscilloscope (a) when it is turned off, (b) reading channel 1, (c) reading channel 2.

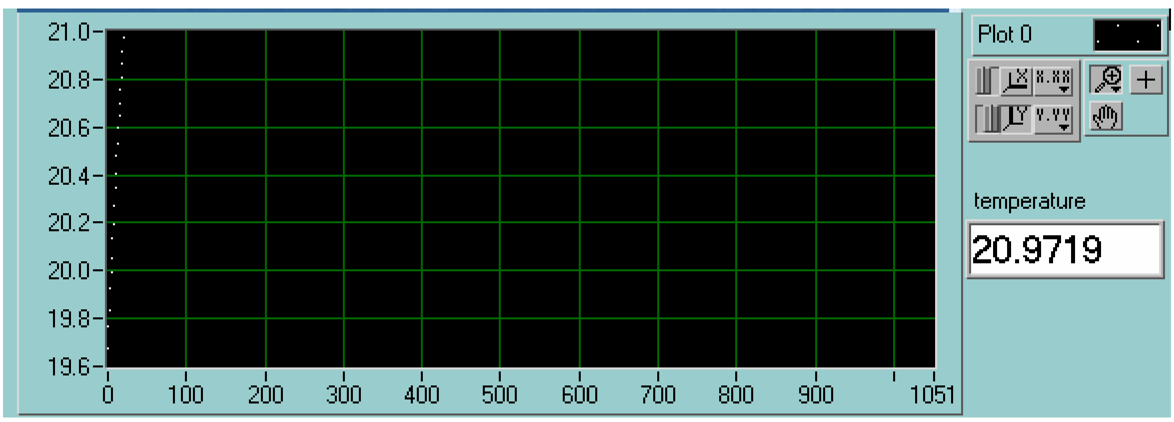

Figure A.5. The graph of the temperature of the LDC

Temperature graph displays the temperature values during the scanning. X-axis is the number of data points taken, and the Y-axis is the temperature value in celcius.

(a)

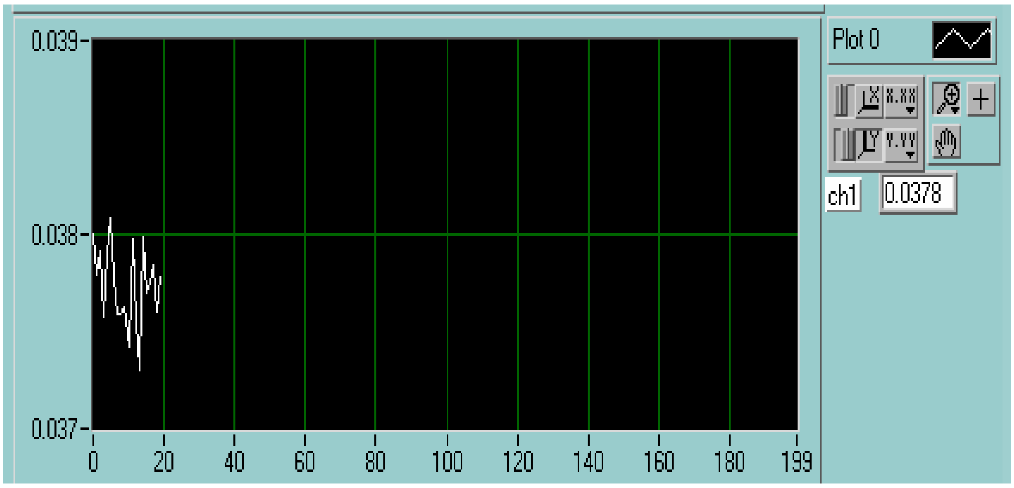

(a)

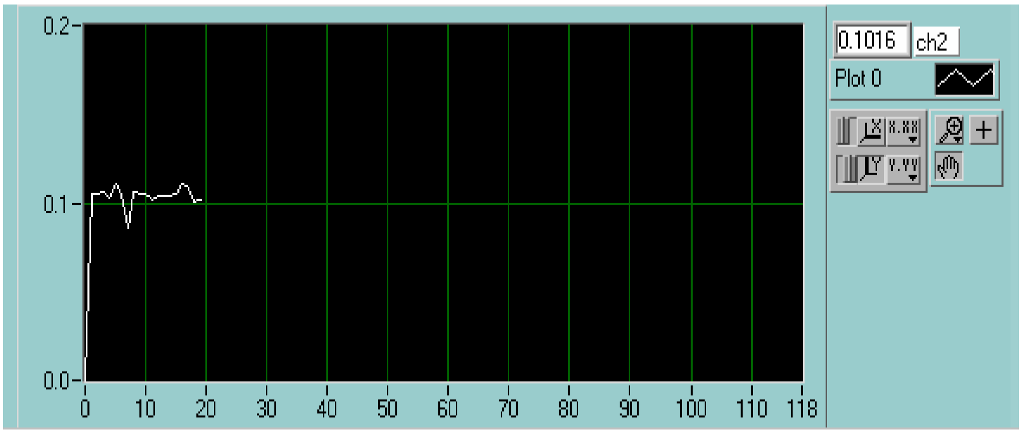

Figure A.6. The graphs of data taken from TDS 210 (a) channel 1, (b) channel 2

The values read from TDS 210 are displayed in Channel 1 and Channel 2 respectively. The X-axis on both graphs represent the number of data points taken.

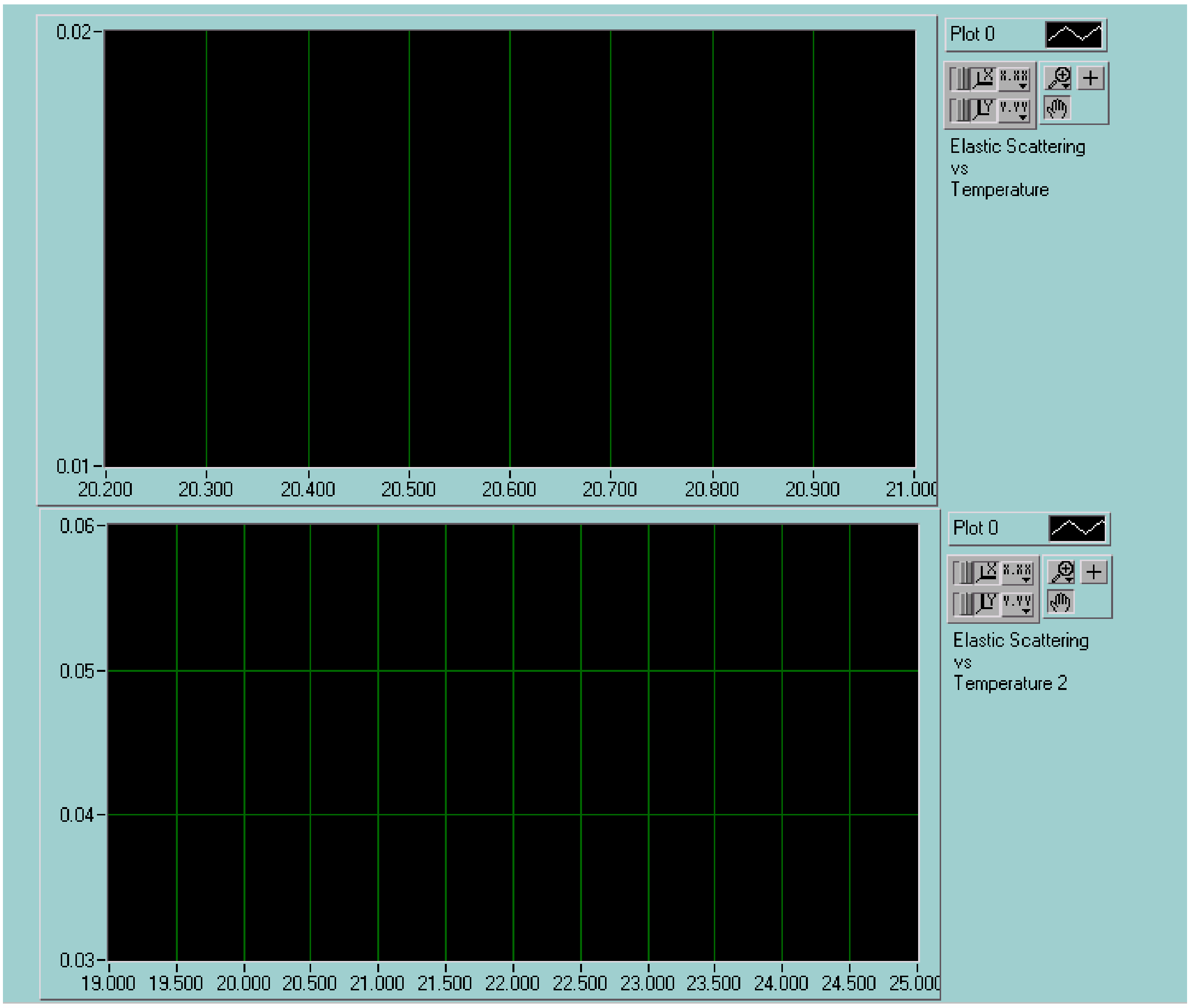

Figure A.7. The graphs of data taken from TDS 210 vs the temperature (a) channel 1, (b) channel 2

These graphs display the TDS reading as a function of Temperature. It will show up at the end of scan process. The graphs display the reading for channel 1 and channel 2 respectively.

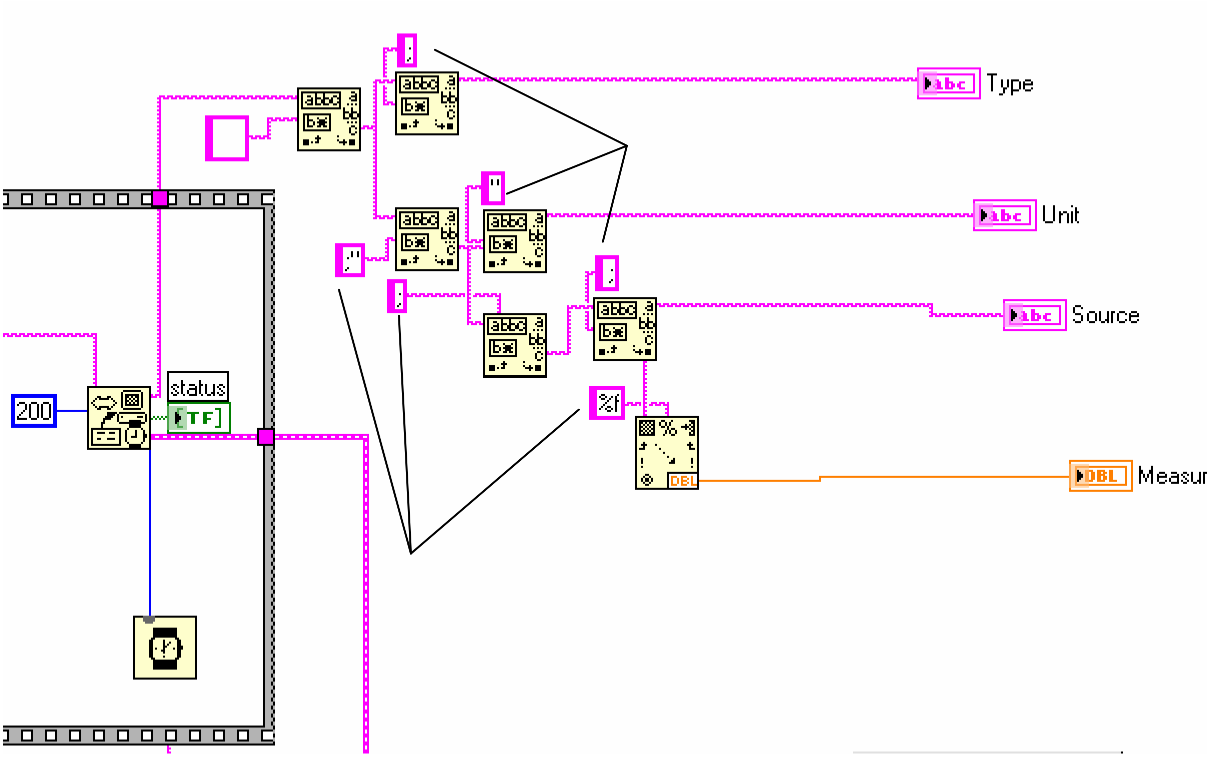

Figure A.8. The diagram of Read Measurement.vi.

This is the diagram of the Read_Measurement_updated.vi. Check the boxes the arrows are pointing. The format inside the boxes should be exactly the same as shown in Figure A.8 otherwise the measurement in the oscilloscope will not be read.

REFERENCES

1. Vahala, K. J., *Optical Microcavities*, World Scientific, Singapore, 2004.

2. Vahala, K. J., "Optical Microcavities", *Nature* 424, pp. 839-846, 2003.

3. Savchenkov, A. A., V. S. Ilchenko, A. B. Matsko, and L. Maleki, "Kilohertz optical resonances in dielectric crystal cavities", *Phys. Rev. A*, vol. 70, pp. 051804, 2004.

4. Cai, M., G. Hunziker, and K. Vahala, "Fiber optic add-drop device based on a silica microsphere-whispering gallery mode system," *IEEE Photon. Technol. Lett*. vol.11, pp. 686-687, 1999.

5. Cai, M., O. Painter, and K. J. Vahala, "Fiber-coupled microsphere laser," *Opt. Lett.* vol. 25, pp. 1430-1432, 2000.

6. Bilici, T., S.Isçi, A. Kurt, and A. Serpengüzel, "Microsphere-based channel dropping filter with an integrated photodetector," *IEEE Photon. Technol. Lett.* vol.16, pp. 476-478, 2004.

7. Yilmaz, Y. O., A. Demir, A. Kurt, and A. Serpengüzel, "Optical Channel Dropping with a Silicon Microsphere," *Photon. Technol. Lett.* vol.17, pp.1662-1664, August 2005.

8. Tapalian, H.C., J.P. Laine, and P.A. Lane, "Thermooptical switches using coated microsphere resonators," *IEEE Photon. Technol. Lett.* vol.14, pp.1118-1120, Aug. 2002.

9. Teraoka, I., S. Arnold, and F. Vollmer, "Perturbation approach to resonance shifts of whispering-gallery modes in a dielectric microsphere as a probe of a surrounding medium," *J. Opt. Soc. Am. B*, vol. 20, pp. 1937-1946, Sept. 2003.

10. Matsko, A. B., A.A. Savchenkov, V.S. Ilchenko, and L. Maleki, “Optical gyroscope with whispering gallery mode optical cavities,” *Opt. Commun.*, vol. 233, pp. 107–112, 2004.

11. Seguin, V. L. and S. Haroche, “Towards cavity-QED experiments with silica microspheres,” *Mater. Sci. Eng.* 48 (1-2), pp. 53-58, 1997.

12. Kuwata-Gonokami, M. and K. Takeda, “Polymer whispering gallery mode lasers”, *Opt. Mat.*, vol. 9, pp. 12-17, Jan. 1998.

13. Ilchenko, V. S., P. S. Volikov, V. L. Velichansky, F. Treussart, V. Lefèvre-Seguin, J.-M. Raimond, and S. Haroche, “Strain-tunable high-Q optical microsphere resonator”, *Optics Comm.*, vol.145, pp. 86-90, Jan. 1998.

14. Serpengüzel, A., S. Arnold, G. Griffel, and J. A. Lock, “Enhanced coupling to microsphere resonances with optical fibers,” *J. Opt. Soc. Am. B* vol.14, pp.790-795, 1997.

15. Vaughan, J. M., *The Fabry-Perot interferometer : history, theory, practice, and applications* Adam Hilger, Bristol, England, 1989.

16. Suzuki, S., Y. Hatakeyama, Y. Kokubun, and S. T. Chu, “Precise control of wavelength channel spacing of microring resonator add-drop filter array,” *Journal of Lightwave Technology*, vol. 20, pp. 745-750, 2002.

17. Yoshida, Y., Y. Nisihhara, “Optical properties and microring laser of conducting polymers with Sn atoms in main chains,” *Journal of Applied Physics*, Vol. 95, pp. 4193-4197, 2004.

18. Armani, D., T. Kippenberg, S. Spillane, and K. Vahala, “ Ultra-high-Q toroid microcavity on a chip,” *Nature*, Vol. 421, pp. 925-929, 2003.

19. Rayleigh, L., "The problem of the whispering gallery," *Scientific Papers 5*, pp. 617, 1912.

20. Barber, P. W. and S. C. Hill, *Light Scattering by Particles: Computational Methods*, World Scientific, Singapore, 1990.

21 Barber, P. W. and R. K. Chang, *Optical Effects Associated with Small Particles* World Scientific, Singapore, 1988.

22. Born, M. and E. Wolf, *Principles of Optics*, Cambridge University Press, New York, 1999.

23. Barber, P. W., R. K. Chang, *Optical Effects Associated With Small Particles,* World Scientific, Singapore, 1988.

24. Sandoghdar, V., F. T. F J. Hare and V. Lefevre-Seguin, "Very low threshold whispering-gallery-mode microsphere laser," *Physical Review A*, Vol. 54, pp. 1777-1780, 1996.

25. Hulst, H.C. van de, *Light Scattering by Small Particles*, Dover, New York, 1981.

26. Bohren, C. F. and D. R. Huffman, *Absorption and Scattering of Light by Small Particles*, Interscience, New York, 1983.

27. Gurvich, I., N. Shiloah, M. Kleiman, "Calculations of the Mie scattering coefficients for multilayered particles with large size parameters," *Journal of Quantitative Spectroscopy & Radiative Transfer*, Vol. 70, pp. 433-440, 2001.

28. Lam, C. C., P. T. Leung, and K. Young, "Explicit asymptotic formulas for the positions, widths, and strengths of resonances in mie scattering," *J. Opt. Soc. Am. B* vol. 9, pp.1585–1592, 1992.

29. Chylek, P., “Resonance structure of Mie Scattering: distance between resonances,” *J. Opt. Soc. Am. A* vol.7, pp.1609-1613, 1990.

30. Guillon, P. and Y. Garault, “Accurate resonant frequencies of dielectric resonators,” *IEEE Transactions on Microwave Theory and Techniques*, Vol. MTT-25, pp. 916-922, 1977

31. Little, B. E., J. P. Laine, and H. A. Haus, “Analytic theory of coupling from tapered fibers and half-blocks into microsphere resonators.” *Journal of Lightwave Technol.* vol.17, pp.704-715, 1999.

32. Pavesi, L. and D.J. Lockwood, *Silicon Photonics: An Introduction*, New York: Springer, 2004.

33. Reed T. Graham and Knights P. Andrew: Silicon *Photonics; An Introduction*, John Wiley and Sons Ltd., West Sussex, 2004.

34. Boyraz, O., and B. Jalali: “Demonstration of a silicon Raman laser” *Opt. Exp.*, vol. 12, pp. 5269-5273, 2004.

35. Coffa, S., M. E. Castagna, M Monaco, A Muscara, and S Loretti, "High efficiency light emission devices in silicon," *Photonics West*, Proc SPIE vol.5366 pp.137-148, 2004.

36. Rong, H. *et al.*, “An all-silicon Raman laser”, *Nature*, vol. 433, pp. 292-294, 2005.

37. Boyraz, O. and B. Jalali, “Demonstration of directly modulated silicon Raman laser”, *Opt. Exp.* vol.13, pp. 796-800, 2005.

38. Rong, H. *et al.*, “A continuous-wave Raman silicon laser”, *Nature*, vol.433, pp.725-728, 2005.

39. Soref, R.A. and B. R. Bennett, "Electro-optical effects in Silicon," *IEEE J Quant Elec* vol.23, pp.123-129, 1987.

40. Cocorullo, G., M.Iodice, and I. Rendina, “All-silicon Fabry-Perot Modulator based on the thermo optic effect”, *Opt. Lett.*, vol. 19, pp. 420-422, 1994.

41. Jacobsen, Rune S. et al. “Strained silicon as a new electro-optic material”, *Nature*. vol 441., 2006.

42. Enderlein, R. and N. J. M. Horing, *Fundamentals of Semiconductor Physics and Devices,* World Scientific, Singapore, 1997.

43. Juin J. L., “Advanced Semiconductor Device Physics and Modeling”, Artech House, London, 1994.

44. Sze, S. M., *Physics of Semiconductor Devices: Second Edition*, John Wiley and Sons, New York, 1981.

45. Sze, S. M., *Semiconductor Devices Physics and Technology*, John Wiley and Sons, New York, 1985.

46. Kasap, S.O., *Principles of Electronic Materials and Devices: Second Edition*, Mc Graw-Hill, Boston, 2002.

47. Serpengüzel, A., S. Arnold, and G. Griffel, “Excitation of Resonances of Microspheres on an Optical Fiber”, *Optics Letters* vol.20, pp.654-656, 1995.

48. Laine, J. P., B. E. Little, D. R. Lim, H. C. Tapalian, L. C. Kimerling, H. A. Haus, “Microsphere resonator mode charachterization by pedestal anti-resonant reflecting waveguide coupler,” *IEEE Photonics Technology Letters*, Vol. 12, pp. 1004-1006, 2000.

49. Gorodetsky, M. L., A. A. Savchenkov, and V. S. Ilchenko, "Ultimate Q of optical microsphere resonators," *Optics Letters* vol.21, pp. 453-455, 1996.

50. Laine, J. P., B. E. Little and H. A. Haus, "Etch-eroded fiber coupler for whispering gallery mode excitation in high Q silica microspheres," *IEEE Photonics Technol. Lett.*, vol. 11, 1999.

51. Serpengüzel, A., S. Arnold, and G. Griffel, *Photonic Atoms: Enhanced light coupling*, in J. Rarity, C. Weisbuch (Eds.) *Microcavities and Photonic Bandgaps : Phyiscs and Applications*, pp. 257-263, Netherlands, Kluwer Academic Publishers 1996.

52. Ansheng Liu *et al.*, "A High-Speed Silicon Optical Modulator Based on Metal-Oxide-Semiconductor Capacitor" *Nature* vol. 427, pp. 615-618, 2004.

53. Xu, Q., B. Schmidt, S. Pradhan and M. Lipson, "Micrometre-Scale Silicon Electro-Optic Modulator", *Nature,* vol. 435, pp. 325-327, 2005.